Porosity and fluid budget of a water-rich megathrust revealed with electromagnetic data at the Middle America Trench

Samer Naif[1,2], Kerry Key[1], Steven Constable[1], and Rob L. Evans[3]

[1]Institute of Geophysics and Planetary Physics, Scripps Institution of Oceanography, University of California San Diego, La Jolla, California, USA, [2]Now at Lamont-Doherty Earth Observatory, Columbia University, Palisades, New York, USA, [3]Department of Geology and Geophysics, Woods Hole Oceanographic Institution, Woods Hole, Massachusetts, USA

Abstract At convergent margins, the distribution of fluids released from the downgoing slab modulates the state of stress and seismic coupling at the megathrust plate interface. However, existing geophysical data are unable to quantify the porosity along this interface. Here we use controlled-source electromagnetic data collected across the Middle America Trench offshore Nicaragua to image the electrical conductivity structure of the outer fore arc. Our results detect a highly conductive channel, inferred to be the region around the décollement, showing the entire section of water-rich seafloor sediments underthrust with the subducting lithosphere. We use an empirical model of the electrical conductivity of porous media to quantify the channel porosity. Our estimates are consistent with sediment compaction studies, showing a rapid decay of 65%–10% porosity from the trench to 25 km landward. We constrain the channel thickness and use the porosity estimates to determine the water budget, which represents the fraction taken up by fluid. The porosity and water budget estimates show significant lateral variations that we attribute to changes in subducted sediment thickness caused by outer rise bending faults. Between 18 and 23 km from the trench, the conductive channel broadens greatly to 1.5–2 km thick, possibly due to concentrated blind faults or sediment underplating, which suggests a sudden change in hydrogeologic structure at the plate interface. The impact of the anomalous conductor on the seismic coupling and mechanical properties of the megathrust is potentially related to the discrepancy in estimated fault slip between seismic and tsunami source inversions for the 1992 Nicaragua tsunami earthquake.

1. Introduction

At subduction zones, a significant amount of water is transported into the crust and mantle [*Thompson*, 1992; *Jarrard*, 2003; *Hirschmann*, 2006]. As a plate is subducted, both mechanical and thermal forces expel water from the downgoing slab [*Peacock*, 1990]. The source and migratory pathway of expelled water modulates multiple tectonic processes [*Hacker et al.*, 2003; *Wada et al.*, 2008; *Wilson et al.*, 2014]. At greater depths, metamorphic dehydration reactions release water into the mantle of the overriding plate, triggering the partial melting that feeds arc volcanism [*Gaetani and Grove*, 1998]. Where temperatures are too cold to generate melt, some of the water is consumed by hydration of minerals in the overriding fore-arc mantle [*Hyndman and Peacock*, 2003]. At shallower depths, expelled water makes its way back to the ocean, contributing to the long-term evolution of seawater elemental compositions [*Kastner et al.*, 1991; *Bebout*, 1995] and promoting gas hydrate formation and other biogeochemical processes that sustain seafloor and crustal microbial communities [*Santelli et al.*, 2008; *Staudigel*, 2014]. Some of the shallow flux migrates through the overriding plate as either diffuse flow or focused flow along faults that feed seafloor seeps, while the remainder flows to the trench along the décollement [*Lauer and Saffer*, 2015].

In the outermost fore arc near the trench, subducted sediments generate the primary flux of expelled water. Rapid burial and tectonic loading mechanically releases pore water by compacting sediments, generating the largest source of escaping fluid from the trench axis to approximately 10–20 km laterally into the margin [*Moore and Vrolijk*, 1992]. These sediments are increasingly loaded and heated as they are transported to greater depths. When temperatures exceed the stability threshold specific to each mineral, the hydrous phases undergo diagenetic dehydration reactions and begin dewatering. By a certain distance from the trench, the flux of water derived from this dehydration eventually surpasses that from compaction, with the position of this transition controlled by the plate convergence rate and the thermal structure of the margin.

Smectite clays, which are prominent in seafloor sediments at a number of margins around the world, contain as much as 20–25 wt % interlayer H_2O and dewater between 60 and 150°C [*Pytte and Reynolds*, 1989; *Moore and Vrolijk*, 1992; *Fitts and Brown*, 1999].

Since seafloor sediments are often highly impermeable, their pore water may remain trapped along the plate interface [*Screaton et al.*, 2002]. The increasing overburden promotes sediment compaction and diagenesis, both of which provide important sources of fluids that generate excess pore pressures, ultimately reducing megathrust fault stability [*Scholz*, 1998; *Saffer and Tobin*, 2011]. An overpressured plate interface has been proposed to induce tremor and episodic slip [*Beroza and Ide*, 2011; *Saffer and Wallace*, 2015], as well as to facilitate rupture to the trench during large to giant earthquakes [*Dean et al.*, 2010; *Kimura et al.*, 2012; *Noda and Lapusta*, 2013]. Geophysical observations confirm that some megathrust earthquakes propagate to the trench seafloor and efficiently generate tsunamis, penetrating what was thought to be a backstop to seismic rupture in the updip aseismic zone [*Satake and Tanioka*, 1999; *Lay et al.*, 2012].

The outer fore arc at subduction zones is marked by either an accreting or nonaccreting margin [*von Huene and Scholl*, 1991]. The hydrogeological conditions and upper plate structure prevalent at each type of margin help to shape the expression of seismogenic behavior through their control on mechanical properties. At accreting margins, some fraction of the sediments on the incoming oceanic plate are scraped off and transferred onto the overriding plate at the trench axis, while the remaining sediments are underthrust with the subducting slab. The accreted sediments that make up the outer fore-arc wedge deform internally over time as more and more material continues to accumulate. Eventually the wedge reaches a critical taper angle, a stability threshold defined by the sum of the seafloor slope and slab dip, where it fails and slides at a steady state [*Davis et al.*, 1983; *Wang and Hu*, 2006]. The critical taper angle depends on the basal coupling at the plate interface, the coefficient of internal friction of the wedge, and the intrinsic strength of the wedge [*Davis et al.*, 1983]. Conditions that are common to most accreting margins yield a large network of fold-and-thrust belts and a gently sloping seafloor.

At nonaccreting margins, most if not all of the incoming sediments are subducted. The lack of frontal accretion coupled with evidence of long-term subsidence and dredged basaltic rock suggests that the fore-arc wedge is more likely composed of crystalline basement that is undergoing basal erosion [*von Huene and Lallemand*, 1990; *von Huene et al.*, 2004a]. Due to the contrasting compositions, the overriding plates of nonaccreting margins likely have far greater internal strength than actively accreting margins. The average taper angle at nonaccreting margins is steeper: 10° compared with 6° at accreting margins [*Clift and Vannucchi*, 2004]. In some margins, such as Nicaragua, the taper angle is thought to exceed 15°. A stronger fore-arc wedge can sustain a steeper angle of repose that possibly accommodates more steeply sloping seafloor, although the impact that the varying hydrological conditions have on the degree of basal coupling and internal friction must also be considered [*Saffer and Bekins*, 2002; *Matmon and Bekins*, 2006].

Another noteworthy distinction between the contrasting margins is the subducted flux of water. The incoming sediment package tends to be significantly thicker for accreting margins, where only the lowermost section is subducted. At nonaccreting margins, the incoming sediments are thinner and a large fraction are subducted. Since sediment porosity drops off exponentially with depth, the high porosity sediments that are scraped off at accreting and underthrust at nonaccreting margins can result in the subduction of up to 1 order of magnitude more water in the latter [*Pichon et al.*, 1993]. Interestingly, several nonaccreting margins exhibit rapid convergence rates, which further add to the net fluid input flux [*Clift and Vannucchi*, 2004]. The steeper taper angle and faster convergence lead to sediments being loaded at a markedly faster rate relative to accreting margins. In conjunction with the considerably larger flux, these observations suggest that nonaccreting margins have the capacity to sustain greater pore pressures and release significantly more fluids into the upper plate along a wide swath of the megathrust plate interface [*Pichon et al.*, 1993; *Saffer and Tobin*, 2011; *Bassett et al.*, 2014].

In this work, we analyze marine controlled-source electromagnetic (CSEM) data collected across the Nicaragua margin to image electrical resistivity and quantify porosity of the upper plate and underthrust sediments. Electrical resistivity is a physical property that is highly sensitive to the bulk fluid content of rocks and hence can be used to constrain porosity. Our characterization of the resistivity structure of the margin provides independent constraints on fore-arc hydrogeology and fluid-tectonic processes that are

complementary to previous results obtained from seismic, magnetotelluric, and geochemical observations [*Hensen et al.*, 2004; *Worzewski et al.*, 2010; *Sallarès et al.*, 2013].

Previously, 1-D CSEM imaging results showed a strong increase in crustal porosity at the trench-outer rise as well as a heterogeneously conductive fore-arc crust, but structural inferences were not possible due to the limits of 1-D interpretation [*Key et al.*, 2012]. Follow on 2-D inversion of the incoming plate data produced a quantitative image at the trench-outer rise displaying conductive bending faults and a gradual reduction in bulk crustal resistivity with proximity to the trench. The results provided observational evidence that bending faults behave as fluid pathways, creating a permeable fabric that significantly hydrates the incoming plate by doubling the amount of water stored in the intrusive oceanic crust [*Naif et al.*, 2015]. Here we focus on a 50 km segment of CSEM data spanning the trench and fore-arc slope.

2. The Middle America Trench

Much of the Middle America Trench is a nonaccreting margin where the incoming sediments are entirely underthrust with the subducting slab [*Ranero et al.*, 2000]. Deep Sea Drilling Project Leg 84 on the Guatemala fore-arc slope discovered an ophiolitic basement, directly observing an upper plate composed of mafic and ultramafic rock of oceanic origin [*Aubouin et al.*, 1984]. Analysis of benthic foraminifera from drill cores also showed evidence for long-term subsidence, which is thought to be caused by tectonic erosion at the base of the upper plate [*Vannucchi et al.*, 2004]. The ophiolitic basement seen off Guatemala has been inferred to persist to the southwest off Nicaragua and northern Costa Rica, where basal erosion may also be occurring [*Ranero and von Huene*, 2000; *Vannucchi et al.*, 2001; *Ranero et al.*, 2008].

Offshore Nicaragua, the 24 Ma Cocos oceanic plate subducts beneath the margin at approximately 80 mm/yr [*DeMets et al.*, 2010]. The plate is covered by about 400 m of sediments that are composed of a top layer of hemipelagic mud with 60 wt % smectite clay and 10 wt % opal, which provide an important source of bound water, and a bottom layer of pelagic carbonate ooze [*Kimura et al.*, 1997; *Spinelli and Underwood*, 2004]. The rapid convergence, large taper angle, and underthrusting of the entire incoming package of water-rich sediments off Nicaragua culminates in a significant flux of fluids to the seismogenic portion of the margin.

Although the Cocos plate off of Nicaragua is relatively young, its thermal state is anomalously cold [*Langseth and Silver*, 1996]. For conductively cooling 24 Ma plate, the surface heat flux is predicted to be about 100 mW/m^2 [*Hasterok*, 2013]. In this case, the dehydration of smectite is expected to initiate less than 10 km landward of the trench where the plate interface is 60°C [*Harris et al.*, 2010]. Offshore northern Costa Rica and Nicaragua, the Cocos plate exhibits heat flow values of less than 30 mW/m^2 [*Hutnak et al.*, 2007]. As a result, the onset of smectite dehydration is delayed until 25 km landward of the trench [*Spinelli et al.*, 2006; *Lauer and Saffer*, 2015].

Some of the water released by compaction and diagenesis flows updip along the décollement and escapes at the trench axis. The fore-arc slope off Nicaragua and Costa Rica is rife with actively venting seeps, with the majority concentrated between 20 and 40 km from the trench [*Sahling et al.*, 2008; *Kluesner et al.*, 2013]. Geochemical sampling of the venting fluids has found tracers that link their source origin to the subducting slab [*Hensen et al.*, 2004; *Tryon et al.*, 2010]. Many of the seeps are associated with faulting, which suggests a significant portion of subducted water escapes by focused flow along faults that cut through the upper plate [*Lauer and Saffer*, 2015].

3. Marine CSEM Survey

Our 280 km long profile consists of 50 ocean-bottom electromagnetic receivers deployed on the incoming oceanic plate, trench, and continental slope offshore of Nicaragua at a nominal site spacing of 4 and 10 km. Each seafloor instrument was equipped with orthogonal pairs of electrodes and induction coil magnetometers to measure the horizontal electric and magnetic fields [*Constable*, 2013]. The broadband instruments are dual-purpose, capable of simultaneously recording CSEM and magnetotelluric (MT) data. All 50 instruments recorded MT data and a subset of 42 stations were located along the portion of the profile where the CSEM transmitter was towed (Figure 1).
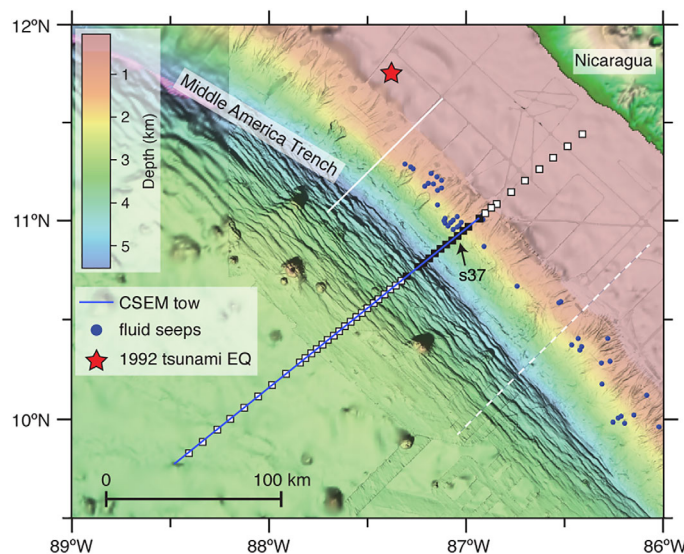
Figure 1. Map of the electromagnetic survey. The faulted seafloor fabric is clearly seen in the high-resolution bathymetric map. The blue line shows the CSEM transmitter towpath. Solid black squares show the location of ocean-bottom electromagnetic receivers whose data we consider here. Data from white squares outlined in black were excluded from modeling. Blue circles show the location of mapped fluids seeps and the star shows the hypocenter of the 1992 tsunami earthquake. The dashed white line is the seismic transect used to constrain the TH1 thermal model [*Ranero et al.*, 2008; *Harris et al.*, 2010] and the solid white line is the seismic and heat flow transect used to constrain the TH2 thermal model [*Walther et al.*, 2000; *Heesemann et al.*, 2009].

The responses that are measured by CSEM and MT data at the seafloor depend on the electric resistivity structure of the underlying material. Since the resistivity of the solid Earth is heterogeneous, the responses are also frequency dependent. Lower frequency transmissions penetrate greater depths and are therefore sensitive to deeper electrical structure. The processed MT data from our survey yield reliable impedance estimates in the 10^{-4} to 10^{-1} Hz frequency band, which are most sensitive to electrical resistivity at upper mantle depths of 20–200 km. This deeper sensing MT data led to the discovery of a melt-rich channel at the lithosphere-asthenosphere boundary [*Naif et al.*, 2013].

In the deep ocean, the high-frequency portion of the passive MT source field is attenuated by the conductive ocean, limiting the ability of MT data to constrain resistivity structure at crustal depth. The CSEM method compensates for the lack of high-frequency energy in the MT data by towing an electric dipole transmitter near the seafloor as an additional source of energy. Our transmitter—the Scripps Undersea Electromagnetic Source Instrument (SUESI)—was outfitted with a 250 m dipole antenna that output a 300 A current. For this survey, SUESI emitted a doubly symmetric source waveform [*Myer et al.*, 2011] with a 0.25 Hz fundamental frequency that provided peak energy in the first, third, and seventh harmonics (0.25, 0.75, and 1.75 Hz). SUESI was deep-towed at a speed of 1.5–2 knots within 100 m of the seafloor to minimize energy losses to the ocean and maximize coupling to the seafloor.

3.1. Data Processing and 2-D Inversion

We Fourier transformed 4 s segments of the time series data, the length of one waveform, to estimate amplitude and phase of the electric and magnetic fields [*Myer et al.*, 2011]. We hand filtered obvious outliers, then robustly stacked these estimates into 120 s bins to increase signal to noise (SNR) and estimate data variance. A 2% error floor was applied to account for uncertainties associated with the geometry and absolute position of SUESI [*Myer et al.*, 2012]. The 120 s stacking windows amount to an amplitude and phase estimate every 90 m (per receiver) since this was the distance travelled by the transmitter in that time. For a detailed description of the processing procedure, refer to *Key et al.* [2012] and *Naif et al.* [2015]. Example data responses for site s37 are shown in supporting information Figure S1.

Our inverted data set includes more than 8200 amplitude and phase estimates from 12 receivers extending 10 km seaward to 40 km landward of the trench. We consider the inline electric field data at three frequencies (0.25, 0.75, and 1.75 Hz). At site s30, we substituted the crossline magnetic field data due to an unusually noisy electric field measurement. The inline electric and crossline magnetic data provide equivalent sensitivity to resistivity structure [*Key*, 2009]. The electric field measurements typically yield higher quality data since the magnetometers are susceptible to vibrational noise and often have lower SNR than the electric field recordings.

We used the open-source MARE2DEM software to invert for electrical resistivity in 2-D with unstructured adaptive finite element grids [*Key and Ovall*, 2011; *Key*, 2016]. The inversion mesh was discretized with about 20,000 quadrilateral elements (supporting information Figure S2) and includes high-resolution
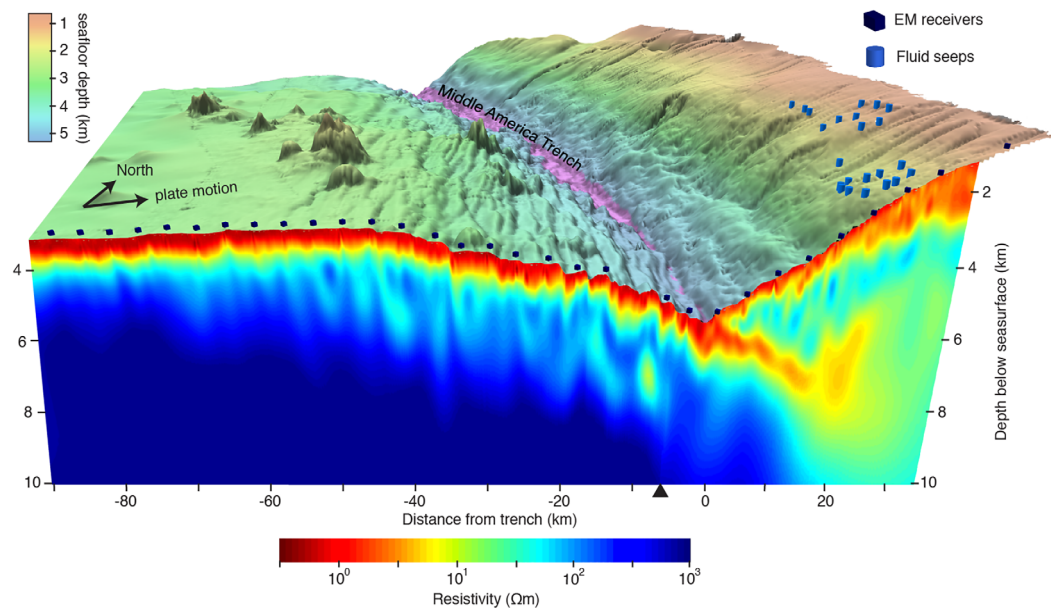
Figure 2. The electrical structure of the Middle America Trench from nonlinear inversion of deep-towed CSEM data. The vertical cross section shows the electrical resistivity structure and the stitched top plot shows seafloor bathymetry. The dark blue cubes show the location of EM receivers. The blue cylinders show the location of active seafloor seeps. The incoming Cocos plate develops several steeply dipping bending faults that correlate with subvertical conductive channels, which significantly hydrate the oceanic crust [*Naif et al.*, 2015]. The channel of low resistivity within the fore-arc margin is caused by subducted sediments. The 1992 tsunami earthquake ruptured this section of the megathrust.

seafloor topography that is essential for getting accurate electromagnetic field responses on the seafloor [*Li and Constable*, 2007]. MARE2DEM employs Occam, an iterative regularized inversion algorithm that searches for the smoothest model which fits the data to a predefined root-mean-square (RMS) misfit [*Constable et al.*, 1987; *de Groot-Hedlin and Constable*, 1990]. For inverse problems where the data errors are accurately known and statistically well behaved (Gaussian distribution), the optimal misfit is RMS 1.0. We inverted for the data in the form of logarithmic amplitude and phase since this form has been shown to be more stable than linearly scaled data when the amplitudes span a few orders of magnitude [*Wheelock et al.*, 2015].

4. Results

The data inversion reached our target misfit of RMS 1.0 in 16 iterations and converged on the smoothest possible model after an additional two iterations. Figure 2 shows a perspective view of the seafloor bathymetry stitched to the final converged electrical resistivity model. We include the inverted resistivity model of the incoming plate [from *Naif et al.*, 2015] for completeness (the location where the two inversion models meet is shown by the black triangle). The electrical structure of the incoming plate and trench is relatively simple, composed of a thin conductive layer that is 500–1000 m thick underlain by an increasingly resistive basement. Approximately 3–4 km landward of the trench, the conductive layer intersects a second conductive layer associated with slope sediments blanketing the fore arc. One branch continues along the fore-arc seafloor while the other dips into the interior of the margin and progressively deepens with distance landward; the region in-between is up to 2 orders of magnitude more resistive.

Figure 3 shows that the dipping conductive channel is congruent with the predicted geometry of the plate interface [*Hayes et al.*, 2012] from the trench axis at the seafloor to 17 km landward of the trench at 4.5 km below the seafloor and exhibits an average taper angle of 11.5°–12° (supporting information Figure S3). From 18 to 23 km into the margin, the conductor diverges from the expected trajectory of the slab and extends 2 km into the overriding plate. Farther landward, the conductor rapidly diminishes to a resistive background, although as discussed below, this is where the data lose the ability to resolve deep structure.

The electrical structure of the margin predominantly reflects the distribution of fluids, where higher resistivity is indicative of lower porosity. Thus, we qualitatively interpret the porosity structure of the margin to be
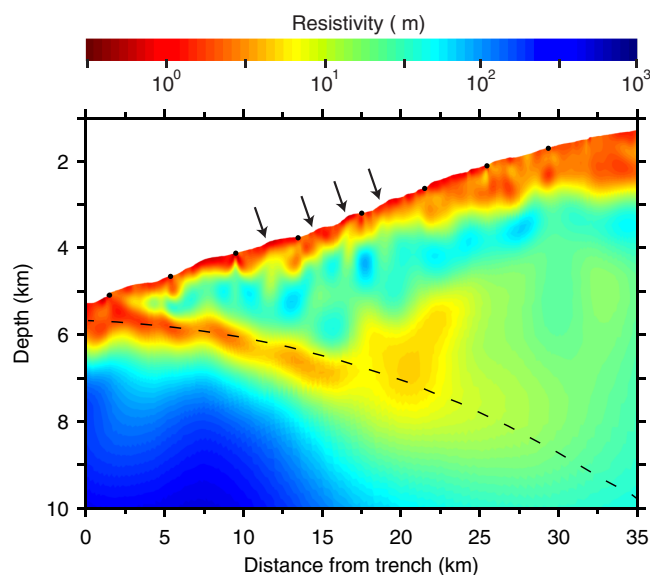
Figure 3. Close up view of fore-arc electrical structure. The channel of low resistivity is caused by subducted sediments that are congruent with the predicted geometry of the plate interface shown by the dashed black line [*Hayes et al.*, 2012]. The arrows point to narrow subvertical conductive channels that correlate with seafloor scarps.

consistent with that of a nonaccreting framework made up of a narrow frontal prism sitting against an upper plate composed of low porosity rock. The simplest explanation for high conductivity features is that they are composed of highly porous seafloor sediments. The 500–1000 m thick conductive seafloor on the fore-arc slope is a veneer of high porosity sediments, and the approximately 500 m thick conductive channel at the base of the low porosity upper plate is caused by subducted sediments that mark the plate interface. The channel of subducted sediments becomes progressively more resistive with distance landward of the trench, which reflects reduced porosities due to compaction.

4.1. Sensitivity Analysis
We construct three representative models with the same bathymetry and data composition as our inversion result to investigate the sensitivity and resolution of the data to the sediment channel conductivity and geometry, as well as other prominent features that we interpret. We calculate forward CSEM responses for the synthetic models, add 2% random noise, and invert the resulting data with a 2% error floor. All of the synthetic inversions converged to RMS 1.0.

The synthetic resistivity models shown in Figures 4a, 4c, and 4e include a conductive layer of seafloor sediments sitting on a resistive upper plate. The seafloor sediment thickness is derived from the real data inversion. The first synthetic model contains a 500 m thick conductive channel that is 1 Ω m. For the second and third synthetic models, the channel resistivity gradually increases with distance from the trench to simulate decreasing porosity with burial depth. The model in Figure 4c includes an upper plate conductor between 18 and 23 km from the trench, and the model in Figure 4e extends the conductor to the seafloor.

The recovered inversion models in Figures 4b, 4d, and 4f show that the CSEM data are highly sensitive to the presence of a conductive plate interface. Beyond 25 km from the trench, the models begin to lose sensitivity at a depth of 8 km below the sea-surface (6 km below the seafloor), which is coincident with the depth to the plate interface. Thus, these synthetic tests confirm that the upward migration and termination of the plate interface conductor and its absolute resistivity are robust model features required by the data and are not artifacts of the inversion regularization or numerical errors.

4.2. Porosity of the Nicaragua Margin
Saline fluids are highly conductive while most rock-forming minerals, at temperatures below 700°C, are highly resistive. Therefore, the bulk resistivity of most porous media is dictated by the bulk porosity and the resistivity of the fluid phase. Empirical relationships are often used to estimate porosity from resistivity measurements, most of which are some form of Archie's law [*Archie*, 1942]:

$$\phi = \left(\frac{\rho_w}{\rho} \right)^{1/m} \tag{1}$$

where ρ is the bulk resistivity, ρ_w is the pore fluid resistivity, ϕ is the porosity, and m is the cementation exponent. The simplified form of Archie's law above is only valid in a fluid saturated medium with a unity-valued tortuosity factor. A constant tortuosity factor of unity reflects a 100% porosity estimate when the bulk resistivity (ρ) is equal to the pore fluid resistivity (ρ_w). Assuming that the pore fluids have the salinity of
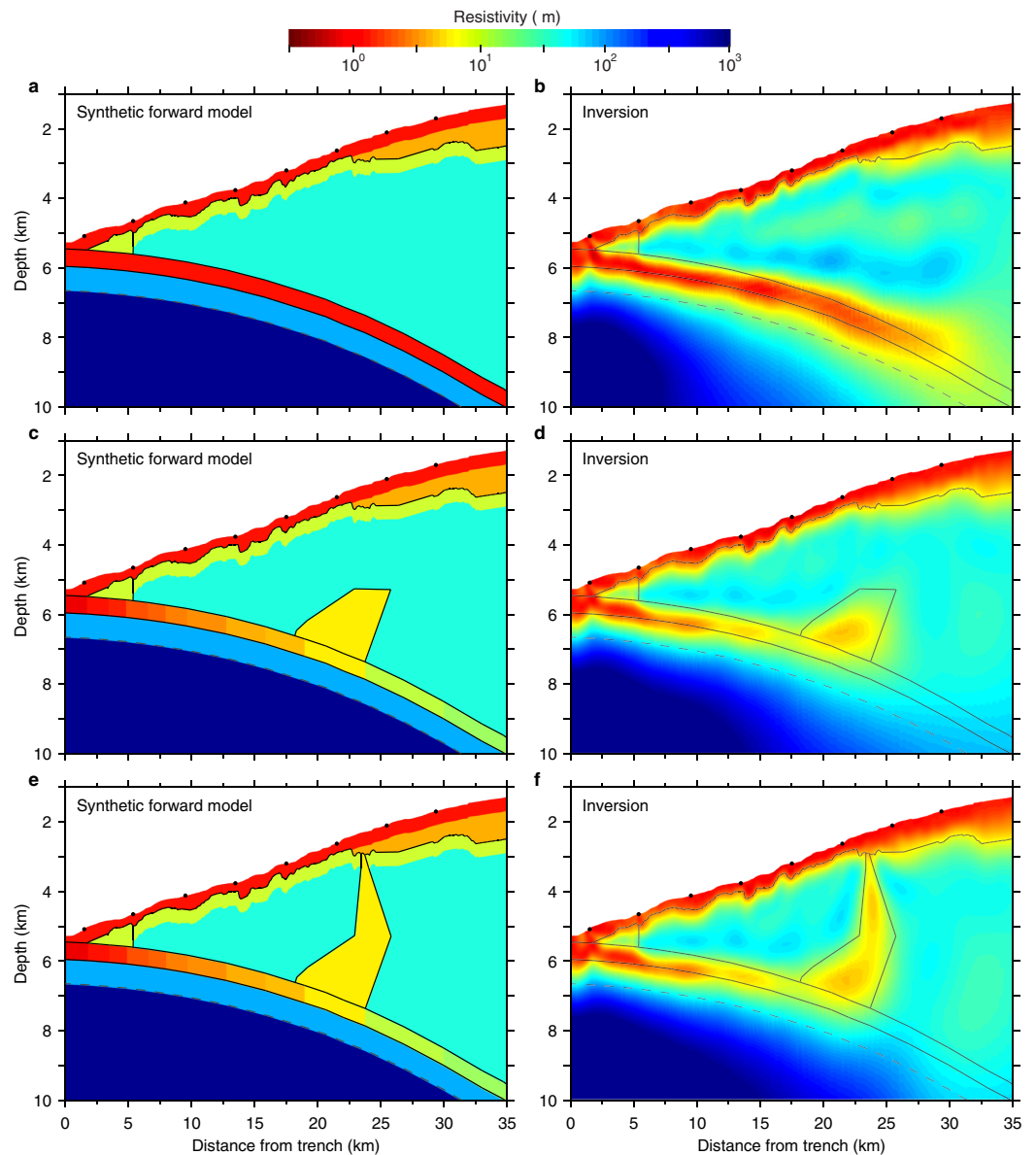
Figure 4. Conductive channel model study. We added 2% Gaussian noise to the synthetic CSEM data generated from the forward models in Figures 4a, 4c, and 4e and inverted to RMS 1.0, yielding the smooth inversion models shown in Figures 4b, 4d, and 4f, respectively.

seawater, we use the cubic relationship from *Constable et al.* [2009] to define the pore fluid resistivity as a function of temperature (between 0 and 200°C):

$$\rho_w(T) = \left[2.903916\left(1 + 2.97175 \times 10^{-2}T + 1.5551 \times 10^{-4}T^2 - 6.7 \times 10^{-7}T^3\right)\right]^{-1} \qquad (2)$$

where T is temperature in degrees Celsius.

Since the pore fluid resistivity depends on temperature, we must consider the thermal structure of the margin when calculating porosity. In the absence of advective heat loss by hydrothermal circulation, global plate-age-dependent cooling models give reliable temperatures of the incoming plate prior to subduction. They are not applicable to more complex thermal settings, such as oceanic plates experiencing advective heat loss or beneath subduction margins. Therefore, we define the temperature in the fore arc with two representative thermal models for Nicaragua, a cold end-member model from *Harris et al.* [2010] (TH1) and the relatively warm model of *Heesemann et al.* [2009] (TH2). TH1 uses fore-arc heat flow values derived from bottom-simulating reflectors imaged off of southern Nicaragua, 80 km southeast of our transect (dashed
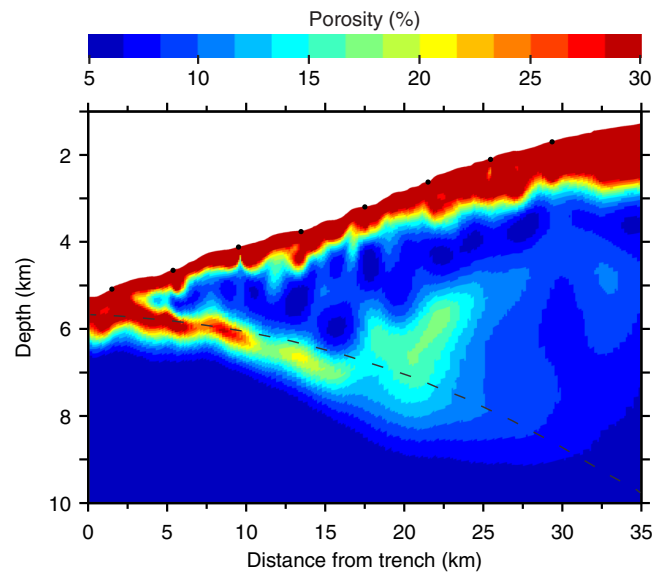
Figure 5. Porosity cross section. We estimated the porosity from the final converged resistivity model with Archie's law for a cementation exponent of $m = 2$ and the warmer TH2 thermal model. The black dashed line shows the plate interface (from Slab1.0).

white line in Figure 1). TH2 uses heat flow derived from bottom-simulating reflectors in addition to heat flow measurements collected off of central Nicaragua, approximately 50 km northwest of our transect (solid white line in Figure 1) [*Grevemeyer et al.*, 2005]. Although both models also account for heat advection in the highly porous/permeable oceanic crust, which extracts additional heat from the margin and yields cooler temperatures, TH1 assumes advection in the incoming plate that persists during subduction while TH2 assumes advection in the incoming plate that ceases at the trench axis. The heat flow observations along the TH2 transect suggest slightly warmer margin temperatures compared with the TH1 transect.

The sediments entering the Middle America margin contain a significant amount of clay minerals [*Aubouin et al.*, 1984; *Kimura et al.*, 1997]. Clays complicate electrical resistivity measurements since they produce a surface conductance that is nonlinearly related to pore fluid salinity [*Waxman and Smits*, 1968]. For an initial estimate of fore-arc porosity, we ignore the contribution of clay conduction and simply use Archie's law to quantify porosity. We will consider the role of clays as we estimate porosity along the décollement in the next section. We use the warmer TH2 thermal model and apply a cementation exponent of $m = 2$, which is representative of sedimentary and fractured igneous rock with generally uniform porosity [*Brace and Orange*, 1968; *Becker*, 1985]. Although this approach overestimates the porosity of clay-rich seafloor and subducted sediments, it also allows us to qualitatively assess the porosity structure of the fore arc by presenting it as a single cross-section image.

Figure 5 shows the porosity structure of the margin. The upper plate of the margin toe, from the trench axis to 3 km landward, is made up of high porosity sediments that make it difficult to determine the depth to the plate interface from the CSEM data. The landward edge of the margin toe sits sharply against the tip of a low porosity layer that gradually thickens with distance from the trench, reaching a thickness of 2.5 km at about 17 km into the margin. With an average porosity of just 10%, we infer this layer to be basement composed of crystalline and/or lithified sedimentary rock.

The basement provides a large porosity contrast that allows us to estimate the thickness of the overlying seafloor sediments and delineate the geometry of the plate interface. We find the seafloor sediments of the fore-arc slope to be 300–600 m thick at 3.5–21.5 km from the trench, then increasing to 1.0–1.2 km thick from 22 km to the landward edge of our CSEM data coverage.

4.2.1. Porosity of the Plate Interface

Estimating porosity with Archie's law is not valid when clay minerals are present because of negative surface charge effects. When hydrated, the clays adsorb water and form a diffuse double layer where cation exchange occurs, which enhances the bulk electrical conductivity [*Revil et al.*, 1998]. Thus, to accurately estimate porosity along the conductive channel of subducted sediments, we use an empirical relationship appropriate for clay-bearing sediments [*Sen and Goode*, 1992]:

$$\phi = \left(\frac{\rho_{bulk}^{-1}}{\rho_w^{-1} + R} \right)^{1/m}, \tag{3}$$

$$R = 1.3\mu_T Q_v + \frac{1.93 m \mu_T Q_v}{1 + 0.7 \mu_T / \rho_w^{-1}} \tag{4}$$

where μ_T is the mobility of counter-ions, Q_v is the clay counter-ion surface charge per unit volume, and m is the cementation exponent. Generally, increasing clay contents correlate with increasing Q_v and m values
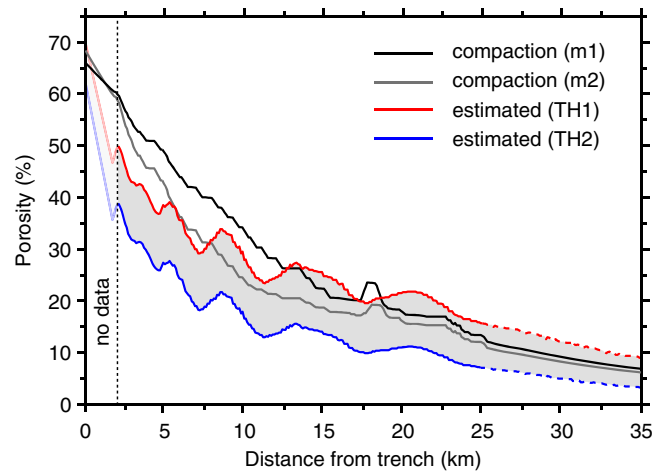
Figure 6. Estimated sediment porosity compared with the independent porosity trend of hemipelagic/pelagic sediment compaction. The black curve (m1) is calculated from the empirical fit of *Lauer and Saffer* [2015], and the gray curve (m2) is from *Spinelli et al.* [2006]. The dashed colored lines beyond 25 km landward of the trench are poorly constrained by the data due to the deeper plate interface depths.

[*Revil et al.*, 1998]. Furthermore, Q_v is a volumetric quantity that increases as a function of increasing porosity at a constant sediment composition. Besides pore fluid resistivity, the counter-ion mobility also varies with temperature:

$$\mu_T = 1 + 0.0414(T - 22) \qquad (5)$$

where T is temperature in degrees Celsius.

We determine the minimum resistivity value within the conductive channel as a function of distance from the trench in 100 m increments and define that to be the bulk resistivity trend of the subducted sediments (ρ_{bulk} in equation (3)). Since there is no clear local minimum beyond 25 km landward of the trench, we use the Slab1.0 model [*Hayes et al.*, 2012] to define a depth target and then average the resistivity within 500 m. We assign the corresponding temperatures from either the TH1 or TH2 thermal models to calculate the pore fluid resistivity (with equation (2)) and clay conductance (with equation (4)). As noted above, empirical analyses dictate that higher m values correlate with higher Q_v (representing higher clay content). The net effect of a higher Q_v is to reduce the porosity estimate relative to a fixed cementation exponent. This applies in reverse, where lower m values correlate with lower Q_v and result in larger porosity estimates relative to a fixed cementation exponent.

Since our knowledge of the clay content, cementation exponent, and counter-ion mobility is limited to the incoming sediments at the trench axis, we consider two sets of values for Q_v and m that are broadly representative of smectite-rich sediments [*Revil et al.*, 1998; *Conin et al.*, 2011]. The upper estimate is calculated with the colder TH1 thermal model, a cementation exponent of $m = 2.6$, and counter-ion mobility $Q_v = 0.3$. The lower estimate is calculated with the warmer TH2 thermal model, a cementation exponent of $m = 2.0$, and counter-ion mobility $Q_v = 0.5$. In contrast to the observed relationship between m and Q_v, we chose to pair a higher m with a lower Q_v (and vice versa) to acquire separate porosity curves that span a wider range of likely values. The two resulting porosity curves are plotted in Figure 6.

Seafloor drilling observations often detect décollement pore fluids that are freshened relative to seawater. By choosing to use seawater salinity (3.5 wt %) to calculate the pore fluid resistivity, we are likely downward biasing our bulk porosity estimates. At the toe of the Costa Rica margin, data from Leg 170 of the Ocean Drilling Program (ODP) show the pore fluid chloride concentration to be freshened by 15%–20% on average relative to seawater, equivalent to 3 wt % salinity. Although this has the effect of increasing the pore fluid resistivity by a similar fraction, it yields a relative porosity increase of approximately 4% in our subducted sediment estimates (e.g., 50% porosity for 3.5 wt % salinity pore fluid is equivalent to 52% porosity for 3.0 wt %). Because there are no in situ measurements of the décollement pore fluid salinity in the outer fore arc of our survey area and the impact of freshened pore fluids on the porosity estimates are muted, we prefer to use the pore fluid resistivity of seawater.

Laboratory-based compaction studies are often used to characterize the porosity of subducted sediments on a regional basis. The compaction porosity is dependent on burial depth. We defined the burial depth as the distance between the minimum resistivity value within the conductive channel and the seafloor, then calculated the compaction porosity with two empirical equations that are constrained by drilling data and consolidation experiments on cores collected at the Costa Rica margin during ODP Leg 170 and Leg 205 [*Spinelli et al.*, 2006; *Lauer and Saffer*, 2015]. Figure 6 shows that the predicted compaction trends are in good agreement with our resistivity-based estimates.
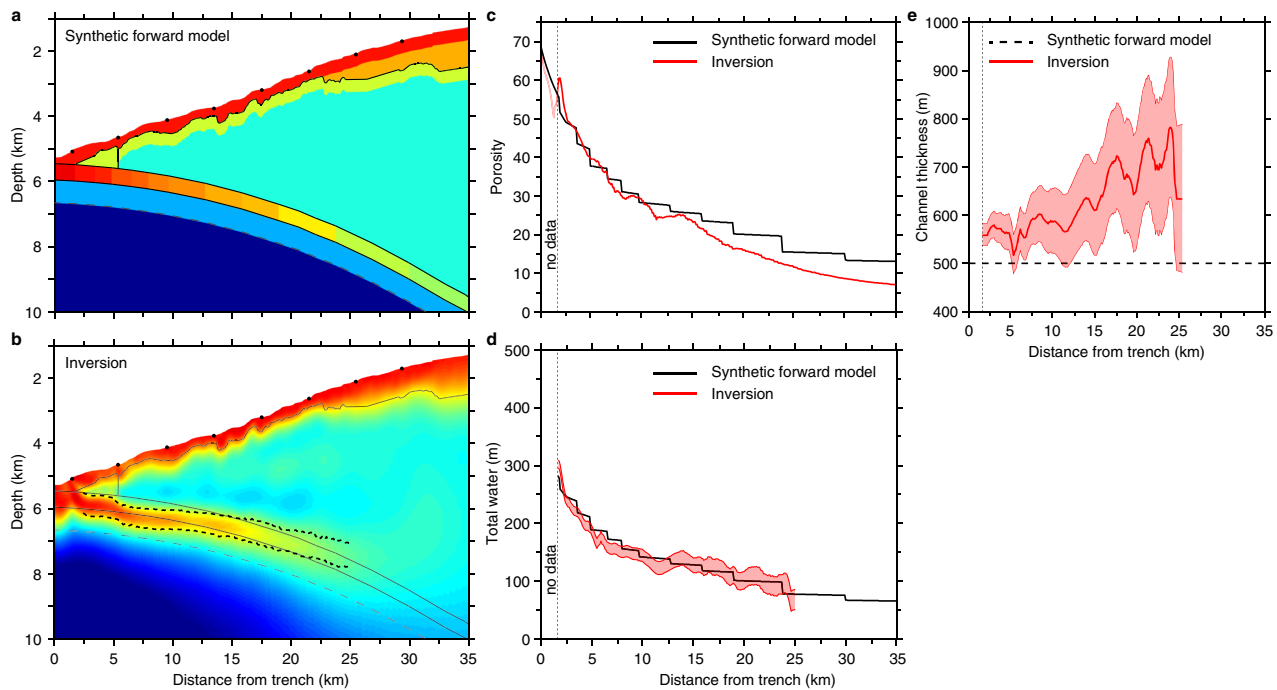
Figure 7. Porosity and total water of synthetic model study. (a) Synthetic forward model. (b) Converged inversion. The dashed black lines show the estimated top and bottom of the channel. (c) Comparison of conductive channel porosity for the synthetic forward model and recovered inversion model. The estimated porosities agree to 15 km landward of the trench, at which point the model sensitivity begins to diminish. (d) Comparison of the conductive channel water budget for the synthetic forward model and recovered inversion model. The estimates are in good agreement from 3 to 25 km landward of the trench. We do not estimate water contents beyond 25 km landward of the trench since the vertical extent of the conductive channel is not clearly resolved. (e) The estimated channel thickness is consistently greater than the true thickness. The error bounds are determined by the vertical resolution of the inversion mesh at the location of the conductive channel (see supporting information Figure S2).

4.2.2. Water Budget at the Plate Interface

Although our inferred porosities are broadly consistent with the compaction-derived trends, our estimates do not constitute an accurate representation of the total water content available at the plate interface. By assuming that the minimum resistivity of the subduction channel is representative of its bulk porosity, we are ignoring its spatial extent. Similarly, since the model resolution diminishes as a function of depth, the inversion regularization may smear and bias the conductive channel to be more resistive. For a thin conductive layer, the data are primarily sensitive to its conductivity-thickness product; thus, the conductive channel is likely smoothed by the inversion to become a thicker but less conductive feature. This is less of an issue near the trench where the plate interface is shallow and thus is well resolved but becomes increasingly important with distance landward and increasing depth.

One way to discern where the model resolution to the subducted sediments begins to diminish is by comparing channel porosities for the synthetic and recovered model pair in Figures 7a and 7b. Figure 7c shows that our porosity estimates for the synthetic forward and inverted models agree to about 15 km landward of the trench, beyond which we increasingly underestimate porosity. Instead, we vertically integrate the porosity to estimate the total water budget of the underthrust sediment package (which we refer to as the plate interface water budget) as a function of distance from the trench. We identify the top and bottom of the channel as the depth where the porosity gradient reaches a local maxima (dashed lines in Figure 7b). Figure 7d compares the water budget of the synthetic forward model, for which both thickness and porosity are known a priori, with the estimated budget of the corresponding recovered inversion model. Although the average channel thickness estimated from the recovered inversion (Figure 7e) consistently exceeds the true 500 m thickness in the synthetic forward model, considering the good agreement between the two water budget curves, our approach accounts for the diminishing model resolution to provide a reliable estimate of the plate interface water budget. The bounds for our channel thickness and water budget estimates are determined from the vertical resolution of the inversion mesh in the vicinity of the conductive channel. The channel thickness uncertainty increases from about 40 m near the trench to 300 m at 25 km landward. The water budget uncertainty, which increases from 15 m at the trench to 35 m at 25 km landward, is the
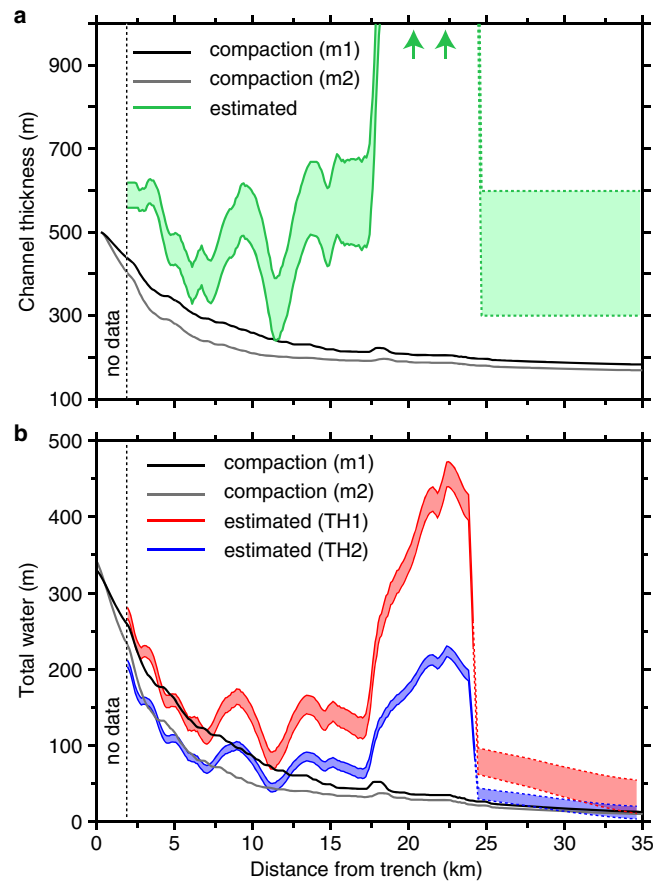
Figure 8. Thickness and total water of subducted sediments. (a) The green curve shows the thickness for the conductive channel of subducted sediments, which is estimated from our inversion result. The black and gray curves show the predicted thickness of subducted sediments undergoing compaction, beginning with 500 m at the trench axis. At 17–24 km, the thickness is more than 1000 m since it includes the anomalous conductor. (b) The blue and red curves show estimates of the plate interface water budget for the real data inversion result. The red curve is calculated with the colder TH1 thermal model, a cementation exponent of $m = 2.6$, and counter-ion mobility $Q_v = 0.3$. The blue curve is calculated with the warmer TH2 thermal model, a cementation exponent of $m = 2.0$, and counter-ion mobility $Q_v = 0.5$. The water content estimates include the entire anomaly (>1.5 km thick at 18–23 km from the trench). The vertical extent of the anomaly must be limited to 400 m for our estimates to be consistent with predictions. The black and gray lines show the predicted water budgets based on the compaction porosity curves from Figure 6.

product of the channel thickness uncertainty and the channel porosity. We omit estimates beyond 25 km landward of the trench since the resistivity and porosity contrasts are too low to reliably determine the thickness or geometry of the conductive channel.

We use the same procedure outlined above to estimate the channel thickness and water budget for the real data inversion. Figure 8a compares our channel thickness estimates with two predictions calculated from the empirically derived compaction porosity curves shown in Figure 6. For the compaction models, we assume a 500 m layer of sediments enters the margin at the trench axis. The rate of thinning depends on the rate that the porosity decays with burial depth; the rapid decay for the *Spinelli et al.* [2006] trend (m2) yields lower water budget predictions relative to the more slowly decaying porosity trend of *Lauer and Saffer* [2015] (m1).

In Figure 8b, we compare our water budget estimates with the two predicted water budgets. Our estimates are in good agreement with the predicted compaction budgets to 12 km landward of the trench. We exclude the water budget in the initial few kilometers of the margin since it is difficult to distinguish the layer of subducted sediments from seafloor sediments of the frontal prism. This region of the model is also less reliable due to a gap in our data coverage; because the transmitter was towed to a maximum depth of 4.95 km, our dipole source was significantly attenuated and did not yield data of sufficient SNR near the trench, where the seafloor is more than 5.1 km deep.

Landward of 12 km from the trench axis, our estimates consistently exceed the predicted compaction budgets. Between 18 and 23 km landward of the trench, if we assume the full vertical extent of the anomalous conductor to be part of the plate interface, our estimates are equivalent to the starting input budget at the trench axis, a discrepancy of 5–10 times more water than predicted from compaction. However, we cannot distinguish the boundary between the plate interface and the upper plate. Our water budget estimates are equivalent to the predicted compaction budget when we arbitrarily limit the vertical extent of the conductive channel that constitutes the plate interface to 400 m thickness. Similarly, limiting the channel to 800 m thick yields water budget estimates that are 2–4 times greater than predicted. This would imply that the remainder of the anomaly, and its water, is within the upper plate. Landward of the conductive anomaly, the porosity contrast between the base of the upper plate and the plate interface is sufficiently small that we cannot clearly resolve the top and bottom of the plate interface. Therefore, although we are confident

that the anomaly does diminish, we cannot accurately estimate the plate interface water budget beyond 25 km.

Note that the predicted compaction budgets ignore the contribution of diagenetic sources, which release an additional flux of water where temperatures span 60–150°C. The TH1 and TH2 thermal models we use to estimate porosity indicate that the plate interface exceeds 60°C at approximately 30 and 17 km from the trench, respectively. Although the TH2 model suggests that diagenetic sources may be significant along our profile, the dewatering flux becomes more prominent farther downdip since the reaction kinetics are primarily controlled by both the absolute temperature and the rate at which temperatures increase. Modeling studies for the Costa Rica margin have considered a range of possible thermal models that consistently show the smectite dewatering flux peaks landward of 30 km from the trench where temperatures are approximately halfway between 60 and 150°C [*Spinelli et al*., 2006; *Lauer and Saffer*, 2015]. The thermal gradient is relatively slow in the TH2 model, with temperatures exceeding 90°C by 31 km landward of the trench. Thus, the diagenetic flux from smectite dewatering is likely a second-order source to at least 25 km landward of the trench. Since the mineral-bound water budget constitutes just 4% of the total sediment input budget [*Spinelli and Underwood*, 2004], we will likely require significant additional sources to compensate for the discrepancy between the predicted compaction budgets and our observed water budgets even if we consider a scenario where the margin is warmer and the diagenetic flux peaks at 20 km landward of the trench.

5. Discussion

5.1. Bend-Faults Modulate Sediment Supply and Water Content at Plate Interface

While our estimates seaward of the anomalous conductor are mostly inline with compaction predictions, Figures 6 and 8 indicate the presence of significant porosity and water budget oscillations that are robust features in the data. The trends oscillate with a characteristic wavelength of approximately 5 km. We attribute this sinusoidal pattern to the subduction of topographic relief. As the incoming plate approaches the trench, it experiences flexure. The bending moment is sufficient to reactivate dormant normal faults that were generated during abyssal hill formation near the ridge axis [*Billen et al*., 2007; *Garcia et al*., 2015]. These reactivated bending-faults are prominent features on the Cocos seafloor at the trench-outer rise, where the 100–500 m scarps are clearly seen in the bathymetry.

The seafloor sediments are offset and undergo erosion and mass wasting due to the accumulated slip along bending faults. As a consequence, the sediment thickness oscillates laterally with a characteristic wavelength of 3–5 km, equivalent to the typical fault spacing. Changes in sediment thickness coincident with faults were also detected in the CSEM data on the incoming Cocos plate, prior to subduction [*Naif et al*., 2015]. Once underthrust into the margin, the varying sediment thickness translates directly to varying water content at the plate interface, which is consistent with the oscillating pattern that we observe in both the porosity and water budget.

We demonstrate the model sensitivity to water budget variations on the plate interface by incorporating topographic relief into the conductive channel of our previous synthetic forward model (Figure 7a) to mimic the effect of bend-faults on the subducted sediment thickness. Figures 9a and 9b show the forward and converged inversion models. Figure 9c shows the corresponding plate interface water budget estimates. The good agreement confirms that our data are indeed sensitive to oscillations in the water budget caused by variable subducted sediment thickness.

5.2. Fluid Pathways and Seafloor Seeps

The structure of the margin appears to be segmented at 17.5 km from the trench by the emergence of the anomalous plate interface conductor. Seaward of the anomaly, we image steeply dipping conductive channels cutting through the resistive basement. They are located beneath seafloor scarps and are approximately 2–3 times more conductive than their surrounding. The most identifiable channels, which have the largest resistivity contrast, also coincide with the largest scarps. Considering their proximity to the seafloor scarps, we interpret these channels to be faults that act as fluid migration pathways. Similarly, *Ranero et al*. [2008] imaged steep seaward dipping normal faults in the fore-arc sediments with bathymetric and
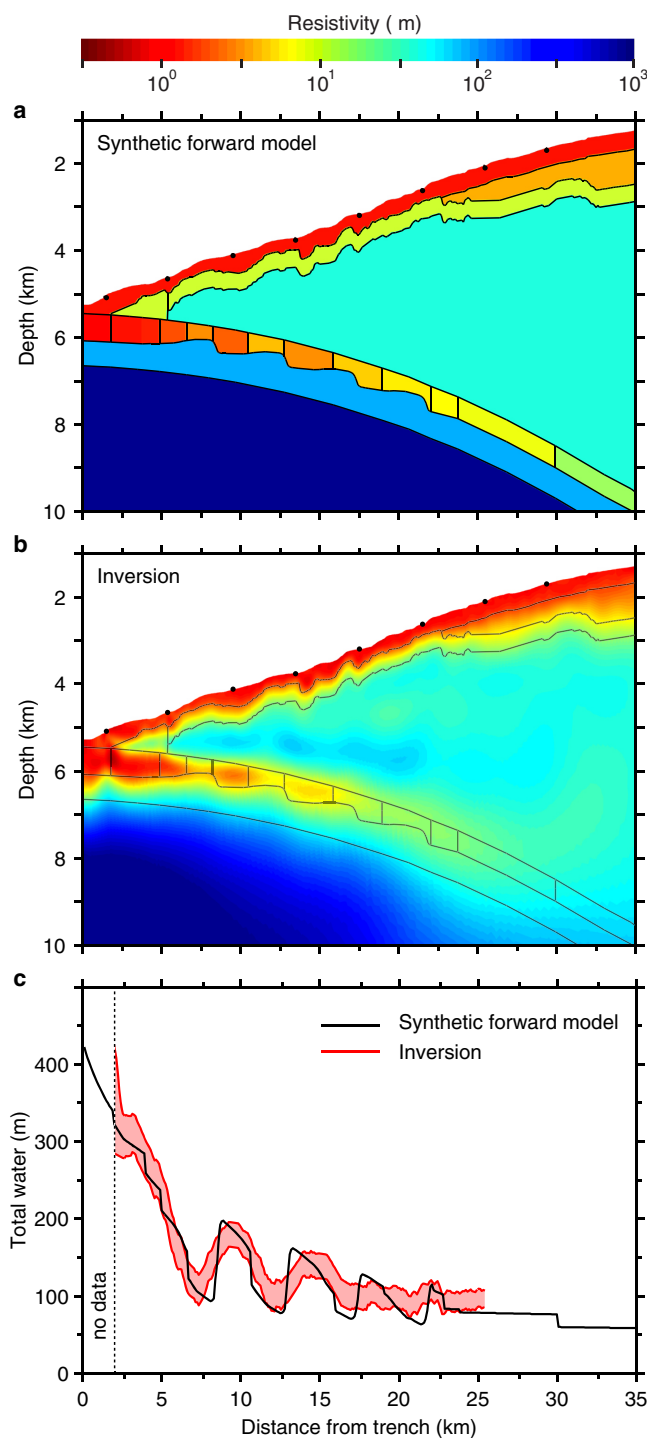
Figure 9. Model study of variable subducted sediment thickness. (a) The synthetic forward model. The conductive channel varies between 300 and 600 m thickness with a 5 km wavelength. (b) The converged inversion. (c) A comparison of the channel water budget for the forward and inverse models. The inversion recovers the oscillating water budget to 17 km landward of the trench, beyond which the variability is too small to be resolved.

multichannel seismic (MCS) data collected off of southern Nicaragua and interpret them to be fluid pathways that possibly extend to the plate interface.

Fluids that originate at the plate interface and exit the system via seeps on the seafloor likely migrate through the upper plate by a combination of diffuse flow and concentrated flow in permeable pathways (e.g., faults). MCS data often image landward dipping splay faults connecting seeps to the plate interface farther downdip, where temperatures are warmer and underthrust sediments release the bulk of their bound water [*Hensen et al.*, 2004]. The source can potentially be determined by the chemical signature of venting fluids, which will be enriched in boron and/or lithium when generated by thermal dehydration of clays. The pore fluids at a number of mound sites across the Costa Rica and Nicaragua margin have been sampled. An actively venting mound with very high flow rates that was discovered 35 km landward of the trench offshore southern Costa Rica, where the incoming plate is significantly warmer, contains highly elevated B and highly depleted Cl and Li concentrations [*Hensen et al.*, 2004; *Tryon et al.*, 2010]. This constrains the source temperature to 85–150°C, thus the fluids originate from farther downdip and must migrate in a seaward trajectory, likely via landward dipping splay faults. The remainder of sampled mound sites, including two located northwest of the Nicoya Peninsula where the incoming plate is anomalously cold, show low levels of Cl depletion but no clear indication of elevated B.

The particular location where the conductive anomaly appears to develop and extend from the plate interface into the upper plate is intriguing, since it overlaps with the dense cluster of active seeps located 22–29 km landward of the trench. The bulk of the anomaly sits 18–23 km landward of the trench and its trajectory places it directly beneath the region where the seeps populate the seafloor. Considering the proximity of our observed conductor to a high concentration of venting seeps, this suggests that some fraction of the
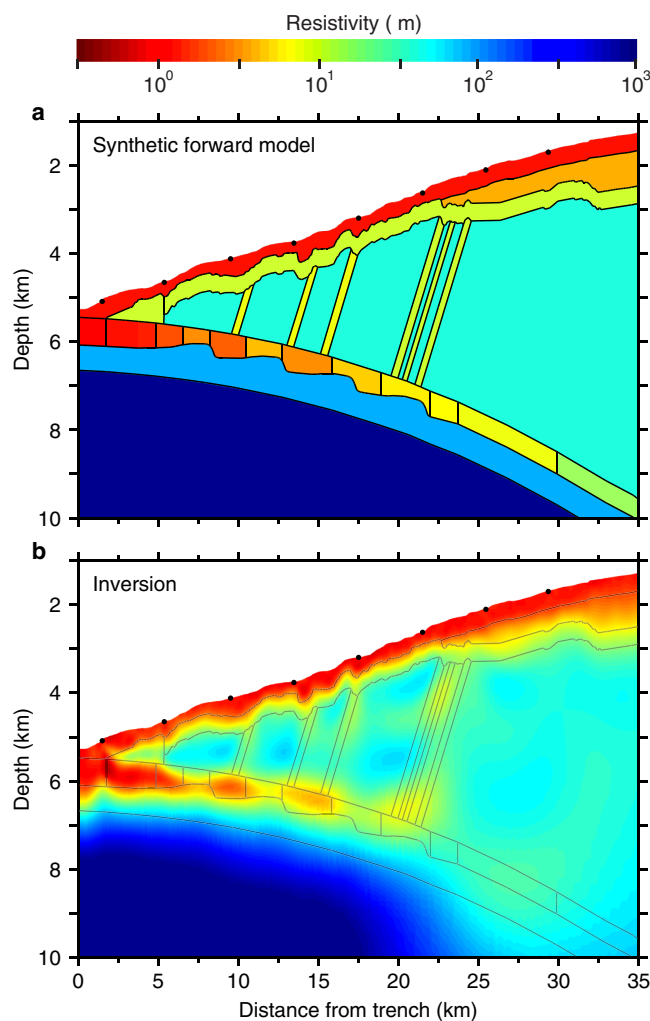
Figure 10. Model study of subvertical conductive channels. (a) The synthetic forward model, which includes three widely spaced subvertical conductive channels seaward of 18 km and three closely spaced channels between 20 and 22 km landward of the trench. (b) The converged inversion, which recovers the subvertical channels, but shows signs of smearing. The three closely spaced channels are recovered as a single conductive feature.

escaping fluids may originate from this anomalous segment of the plate interface. Assuming the seeps here are partially fed by the conductive anomaly beneath our profile, such fluids would then be sourced updip and hence must migrate landward, possibly along seaward dipping faults. In that case, the source of the fluids would be compaction since the TH1 and TH2 thermal models indicate that the temperatures are too cold near the anomaly to generate a clay dehydration flux. This may explain why some mounds do not show signs of elevated B. However, we cannot rule out that clay dehydration fluids also feed these mounds since they happen to exhibit significantly slower flow rates, which allows additional time for dilution of B by adsorption in seafloor sediments as well as by convective mixing with seawater. Additional chemical analysis for the cluster of seeps along our profile is required to determine the origin of their venting fluids.

5.3. The Anomalous Conductor: Comparisons With Bathymetry and MCS

Interpreting the conductive anomaly to be a single unit would suggest it is too broad to be caused by a fault. However, the anomaly may be smeared by the inversion regularization. To sharpen it, we must increase its conductivity in order to conserve its conductivity-thickness product. A sharper more conductive feature also requires greater porosity. Considering that the porosities already exceed 15%, we consider a sharper anomaly unlikely. Alternatively, to account for both the bulk conductivity signature and relatively wide spatial extent, the anomaly may be caused by multiple closely spaced conductive channels that our data are not able to resolve.

Using 3-D MCS data, *Bangs et al.* [2015] imaged steep seaward dipping thrust faults that cut through the overriding plate offshore of Osa Peninsula (400 km SE), at approximately the same distance into the margin as our anomaly. Because these thrust faults coincide with a sudden reduction in the reflection amplitude of the plate interface, the authors interpret them to behave as fluid pathways that drain the plate interface. This may also be occurring off of Nicaragua, in which case thrust faults would be responsible for the conductive anomaly. However, the top of our anomaly is separated from the base of the seafloor sediments by a 1.5 km thick resistive (low porosity) basement. This contrasts with the nature of the steeply dipping channels that are evident seaward of 18 km from the trench; they are more conductive near the surface relative to greater depths, while also extending from the plate interface to the seafloor. Although their absolute conductivity is less than that of the anomaly, we might expect a similar behavior if the anomaly were caused by seaward dipping faults.

We modify the previous synthetic model (Figure 9a) to include three steeply dipping conductive channels spaced 2–3 km apart as well as a set of three closely spaced channels located at the same distance from the trench as our anomaly (Figure 10a). The inversion (Figure 10b) is able to recover the widely spaced channels

with some smearing and a similar pattern to the real data inversion of higher conductivity near the surface diminishing with depth. The three closely spaced channels are recovered as a single conductive feature that also extends all the way to surface. Therefore, the real data cannot distinguish between a single conductive channel and several closely spaced channels but are clearly sensitive to the resistive gap between the top of the anomaly and the base of the conductive seafloor sediments. Considering that the anomaly is both highly conductive and does not extend to the seafloor, it suggests that multiple blind faults or some other nonfaulting mechanism may be responsible.

Besides faulting, additional mechanisms that enhance porosity (and hence conductivity) at the base of the overlying plate include underplated sediments, seamount subduction, or hydraulic fracturing, all of which have distinct bathymetric signatures associated with them. We plot the regional fore-arc bathymetry [*Weinrebe and Ranero*, 2012] in Figure 11 to help distinguish the cause of the anomaly.

At a typical convergent margin, we would expect the outermost fore-arc seafloor to exhibit the steepest slope, gradually shallowing with increasing distance from the trench until becoming nearly flat at the edge of the continental shelf. Instead, we see a coherent steepening in the middle slope along a wide swath of the Nicaragua fore arc. In the event that a seamount is subducted, the fore-arc seafloor directly above is uplifted and a clear wake of erosion and mass wasting is left behind in its trail [*Dominguez et al.*, 1998; *Ranero and von Huene*, 2000]. The lack of any such bathymetric indicators near our CSEM transect rules out a subducted seamount as the origin of the anomaly.

The unusual slope behavior in the region has been noted in previous work [*von Huene et al.*, 2004b; *Harders et al.*, 2011]. *Von Huene et al.* [2004b] attribute the steepened middle slope to either subsidence by erosion or uplift by sediment underplating. The authors preferred an erosional mechanism since it is more consistent with independent observations of long-term subsidence and crystalline fore-arc basement offshore of Guatemala, which has been inferred to extend southeast to Costa Rica [*Vannucchi et al.*, 2001, 2004].

MCS data collected offshore of southern Nicaragua imaged a high amplitude negative polarity reflector at the plate interface that indicates the presence of trapped fluids. *Ranero et al.* [2008] infer that the trapped fluids are highly overpressured and hydraulically fracture the base of the overriding plate. Under such circumstances, material fragments loosened during fracturing are then transferred to the subducting slab and transported to depth, consistent with proposed erosional margin processes [*von Huene et al.*, 2004a]. This would lead to seafloor subsidence directly above the region of hydraulic fracturing.

If our anomaly, which thickens toward the coast, reflects a zone where hydrofracturing and basal erosion is ongoing, the seafloor should subside between 18 and 23 km from the trench and create steeper bathymetric slopes landward of 22–23 km. Alternatively, if we infer either underplated sediments or steep seaward dipping faults, the seafloor will be uplifted above the anomaly, steepening the fore-arc seaward of
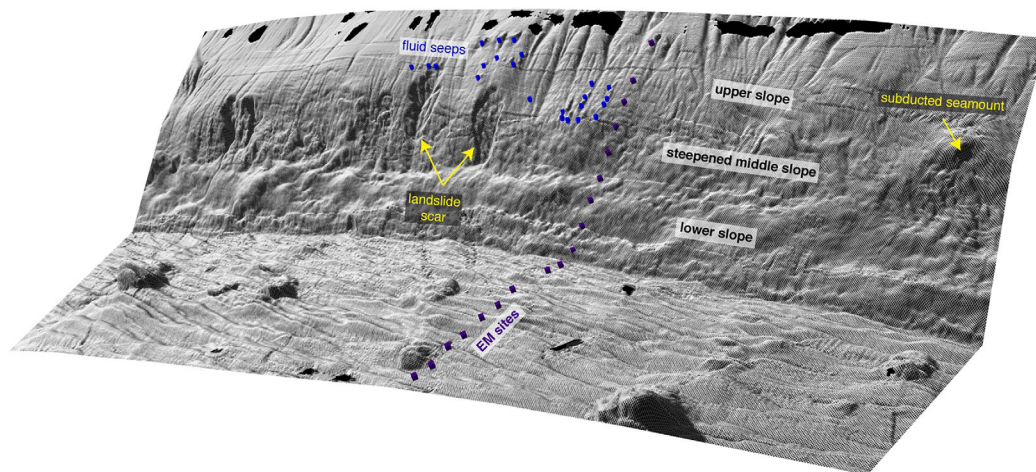

Figure 11. A perspective view of the fore-arc slope offshore of Nicaragua. The steepened middle slope can be tracked for more than 100 km along strike. A subducted seamount on the right side of the map shows a distinct bathymetric expression that is not seen in the immediate vicinity of our EM profile. Bathymetry data from *Weinrebe and Ranero* [2012].
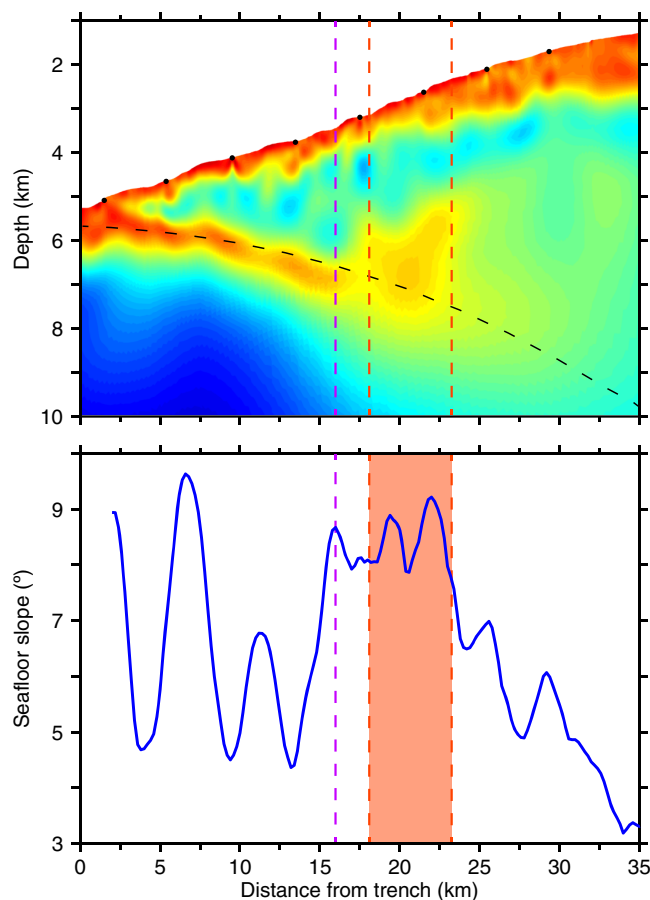
Figure 12. Fore-arc seafloor slope angle. The Nicaraguan fore arc is much steeper than typical accreting margins. Between 16 and 23 km landward of the trench, the seafloor slope peaks at 8–9°, which exceeds the average steepness of the lower slope (seaward of 15 km). The location of the steepened seafloor relative to the conductive anomaly is consistent with uplift by underplated sediment or steep seaward dipping faults.

22–23 km. We use depth sounding data (submeter accuracy) measured with SUESI's auxiliary sensors to calculate the seafloor slope along our profile (Figure 12). The steepened middle slope reaches a peak angle of 9° at 20 km into the margin. Since this is seaward of 22–23 km, we rule out basal erosion as the cause of the anomaly, which leaves either sediment underplating or blind faults as explanations.

5.3.1. Sediment Underplating

A number of depth-migrated MCS transects located offshore of Costa Rica have imaged enigmatic features referred to as "megalenses" [*Shipley et al.*, 1992; *McIntosh et al.*, 1993; *Ranero and von Huene*, 2000]. They occur along the plate interface and are typically 5–15 km wide by 1–2 km tall. For MCS lines located off Nicoya Peninsula, *McIntosh et al.* [1993] interpreted such megalens features as sediment underplating and noted that they correlate with steepened bathymetry and steepened basement ramps at the base of the seafloor sediments. An MCS line that is nearly coincident with our CSEM line also shows a similar steepened basement ramp between 16 and 24 km landward of the trench that correlates with the steepened seafloor bathymetry, exactly above the location of our conductive anomaly [*McIntosh et al.*, 2007]; it is difficult to assess whether there are seismic structures that corre-

late with our conductive anomaly since the MCS image is distorted by the seafloor multiple there. In contrast, *Ranero and von Huene* [2000] considered the lack of significant uplift associated with the vertical scale of megalenses to indicate that they are material that is transferred from the base of the upper plate to the lower plate. This is problematic since the material should then proceed to subduct as part of the lower plate, whereby it would generate uplift and a wake of seafloor disruption in the same fashion as subducting seamounts. Instead, underplating would cause isolated uplift in the zone where material is transferred to the upper plate.

Geologic and seismic observations identify structures that are interpreted as sediment underplating at a variety of subduction margins and ancient accretionary complexes [*Platt et al.*, 1985; *Sample and Fisher*, 1986; *Kimura and Mukai*, 1991; *Park et al.*, 2002; *Clift and Hartley*, 2007; *Collot et al.*, 2008; *Scherwath et al.*, 2010]. Underplating is thought to occur during the formation of thrust duplexes [*Brandon*, 1984; *Cowan*, 1985]. Similar interpretations were proposed for the Middle America margin as well [*Moore et al.*, 1982; *Silver et al.*, 1985; *McIntosh et al.*, 1993]. Duplex formation is not expected to significantly deform the slope sediments or produce widespread faulting, which is consistent with the lack of conductive channels above our anomaly as well as the limited scale of bathymetric uplift relative to the dimension of observed megalenses. Another factor that warrants further consideration is the potential change in effective normal stress at the plate interface that would likely accompany the emergence of the conductive anomaly, as this could locally impact the taper angle and hence the seafloor slope [*Davis et al.*, 1983; *Wang and Hu*, 2006].

Underplating also occurs where the subducting slab meets the crust-mantle boundary of the overriding plate. Some of the subducted sediments may accumulate there if they are too buoyant to be transported to greater depths [*Bassett et al.*, 2010]. Here the proposed underplating is occurring at shallow depths. One possibility is that the edge of our conductor abuts denser upper plate material. *Walther et al.* [2000] analyzed wide-angle seismic data from a transect approximately 50 km northwest of our CSEM survey, where the middle slope is also steepened. Their forward velocity model is superimposed on colocated seismic reflection data and shows a boundary at 30 km from the trench that sits near the base of the upper plate. It separates slower material seaward (4.5–5 km/s) from faster material landward (5.8 km/s). The seismic boundary is equivalent with a density increase from 2.6 g/cm^3 material to 2.9 g/cm^3 material (see Figures 3, 4, and 11 from *Walther et al.* [2000]) If such a feature extends along the margin beneath our profile transect, it may facilitate duplexing or even act as a density filter in the same manner as the continental Moho.

Geochemical data from arc volcanoes in Nicaragua suggest highly efficient recycling of hemipelagic seafloor sediments to the mantle wedge, which argue against sediment underplating [*Patino et al.*, 2000; *Carr et al.*, 2007]. This contrasts with the Costa Rica arc, which is relatively depleted in such tracers and hence suggests sediment underplating [*Morris et al.*, 2002]. Underplating along the Costa Rica margin is also supported by evidence for Quaternary coastal uplift [*Fisher et al.*, 1998; *Sak et al.*, 2009]. Furthermore, wide-angle seismic data image a feature at 15 km depths along a 50 km long segment southeast of the Nicoya Peninsula interpreted to be underplated material [*St Clair et al.*, 2016]. A phase of underplating along the Nicaragua margin would need to occur within the last 1–1.5 million years or in short pulses to not impact the present day volatile tracers emitted at the arc. This is possible since Quaternary uplift is also observed at the outer high offshore Nicaragua [*Ranero et al.*, 2000]. Considering the evidence for long-term margin wide subsidence, the uplift is likely occurring locally or initiated recently.

5.3.2. Impact on the Megathrust

Regardless of the anomaly's underlying cause, its existence implies a sudden change in the hydrogeologic properties of the plate interface. The smectite-rich sediments and the highly porous and altered extrusive oceanic crust transport a significant volume of interstitial and mineral-bound water, capable of contributing to extreme overpressure development [*Kameda et al.*, 2011; *Saffer and Tobin*, 2011]. Furthermore, the reservoir of crustal water is amplified by bending faults at the outer rise [*Naif et al.*, 2015].

The abundant availability of water at the plate interface suggests that the subducted sediments form a continuous albeit variably overpressured zone, lowering the effective normal stress along a large swath of the megathrust extending from the trench to 18 km landward. At that point the décollement is disrupted, possibly due to sediment underplating or concentrated faulting, changing the fluid structure of the megathrust farther downdip. Since the margin is thought to be fairly cold, sediment dewatering is expected to impact pore pressures beyond 25 km from the trench axis [*Lauer and Saffer*, 2015]. As such, the hydrogeologic structure that regulates the effective normal stress and hence plate coupling along the Nicaragua megathrust can be split into three distinct sections: an updip zone that is decoupled and dominated by sediment compaction, a relatively coupled transitional zone where the conductive anomaly resides and the décollement is likely disrupted and drained, and a downdip zone where mineral dehydration reactions modulate coupling.

The nature of the 1992 Nicaragua tsunami earthquake (M$_w$ 7.6), which ruptured the margin where our survey was located, is related to the abundance of water that we observe at the megathrust. The source spectrum of this event was highly depleted in the short period band, the estimated stress drop was just 0.08 MPa, the total energy radiated relative to the seismic moment magnitude is the lowest on record, the rupture speed was slow (1.6 km/s), and aftershock activity was noticeably absent within 40 km of the trench axis [*Kanamori and Kikuchi*, 1993; *Ye et al.*, 2013]. All of these factors suggest a weak megathrust, which is consistent with a water-rich plate interface filled with weak clay-bearing sediments.

The details of the rupture are potentially linked to our observed anomaly. The epicenters of radiated energy vary systematically as a function of frequency: the lowest frequency energy is concentrated nearest to the trench, with higher frequencies located at progressively increasing distances into the margin [*Ihmlé*, 1996]. The 1999 Chi-Chi and 2011 Tohoku-oki megathrust earthquakes also show an inverse correlation between the amount of slip and the high-frequency energy radiated [*Ma et al.*, 2003; *Meng et al.*, 2011; *Yao et al.*, 2011]. In addition, *Ye et al.* [2013] present a seismic source inversion model of the Nicaragua event showing about 1 m of peak slip between 20 and 80 km from the trench that diminishes toward the trench axis. The

area of peak slip is inferred to be a zone of high plate coupling. In contrast, a tsunami source inversion of runup heights measured at the coastline and tidal gauge records requires 3 m of slip to reach the trench axis [*Satake*, 1994].

The megathrust segmentation that we inferred from our observed conductive anomaly may explain the discrepancy between seismic and tsunami source inversions as well as the spatial pattern of radiated energy. During the rupture, the zone updip of the anomaly radiated highly depleted high-frequency energy. Since tsunami source inversions require up to 3 m of megathrust slip to the trench axis, this suggests that the rupture here was seismically "quiet," consistent with a decoupled megathrust. The rupture along the megathrust downdip of our conductive anomaly, which is where seismic source inversions place the main slip patch, radiated more high-frequency energy. This is consistent with our interpretation of higher plate coupling downdip of the anomaly. Interestingly, the seaward edge of high plate coupling inferred from the seismic source inversion of *Ye et al.* [2013], although poorly constrained, happens to coincide with the position of our anomaly.

6. Conclusions

We collected marine CSEM data across the trench-outer rise and fore-arc slope offshore of Nicaragua to image the electrical resistivity structure of the upper plate and subducting slab. We applied a 2% error floor and inverted the high quality data with MARE2DEM, a 2-D numerical solver. Our final converged inversion clearly imaged a highly conductive channel of subducted sediments from the trench axis to 25 km into the margin that is congruent with the predicted geometry of the plate interface. At 18 km landward of the trench, the channel suddenly begins to thicken until it reaches a maximum thickness of 1.5–2 km at 23 km from the trench. Overlying the conductive plate interface is a resistive basement and a veneer of conductive seafloor sediments. The low porosity basement is occasionally cut by narrow subvertical conductive channels that connect with seafloor scarps and thus are likely caused by fluid pathways along fault damage zones.

The proximity of the anomaly to a cluster of actively venting seeps and mud mounds suggests it may be a reservoir from which the escaping fluids are sourced. This is contradicted by the thick resistive gap seen between the seafloor sediments and the top of the anomaly. If the fluids are indeed sourced from the anomaly, then the lack of subvertical conductive channels linking the anomaly to the seafloor implies either diffuse fluid migration or concentrated pathways too narrow for our data to resolve, or a combination of both.

We quantified porosity from the electrical resistivity inversion. The porosity of the conductive channel decays exponentially with distance landward from 65% at the trench axis to 10% at 25 km into the margin, which is consistent with laboratory predictions [*Spinelli et al.*, 2006; *Lauer and Saffer*, 2015]. We integrated the porosity within the channel to calculate the total water content as a function of distance from the trench. Our water budget is also mostly consistent with the predicted budget for 500 m of subducted sediments, but contains significant oscillations with 4–5 km wavelength. The wavelength of the oscillations is similar to the characteristic spacing between bend-faults on the incoming plate. Thus, the oscillations reflect variations in the thickness of subducted sediments that are caused by changes in basement topography during bend-fault generation at the trench-outer rise.

The thickened channel at 18–23 km from the trench requires high porosities. If we assume its full extent constitutes a part of the plate interface then the subducted water budget would exceed predictions by up to an order of magnitude. A large fraction of the anomaly is more likely located within the overriding plate since it is difficult to explain such a sudden and significant increase in the plate interface water budget. Some mechanisms that potentially explain the cause of the anomaly include concentrated faulting, underplated sediments, or hydraulic fracturing. The seafloor slope directly above the anomaly is steepened and suggests localized uplift. This rules out basal erosion via hydrofracturing, although it is still possible that the anomaly reflects a damage zone caused by fracturing that is not associated with basal erosion and seafloor subsidence. Furthermore, there is a 1.5–2 km thick resistive gap between the top of the anomaly and the base of the seafloor sediments, which limits a faulting interpretation to a scenario with concentrated blind faults. Sediment underplating can explain both the high porosities, the localized bathymetry uplift, and the steepened basement ramp at the base of the slope sediments. However, it is not clear what mechanism

would be responsible for underplating, or if underplating is even possible considering the large vertical aspect ratio of the anomaly (1.5–2 km tall and 6–7 km long). The scale of the conductor resembles megalens features that have been imaged seismically [*Shipley et al.*, 1992; *McIntosh et al.*, 1993; *Ranero and von Huene*, 2000], which suggests that the two are related. The underplating may damage the overlying plate, which would thicken the appearance of our anomaly.

Our survey was located within the region that ruptured during the 1992 Nicaragua tsunami earthquake [*Ye et al.*, 2013]. The spectrum of radiated seismic energy was highly depleted in the high-frequency band, which is consistent with our observation of water-rich sediments at the plate interface [*Kanamori and Kikuchi*, 1993; *Ihmlé*, 1996]. Additionally, there is some discrepancy between seismic and tsunami source inversions regarding the magnitude and spatial extent of fault slip during the rupture [*Satake*, 1994; *Ye et al.*, 2013]. While the cause of our anomaly remains unclear, it suggests sudden changes in the hydrogeology of the plate interface (and hence the seismogenic properties of the megathrust). This change may mark the transition from a seismically decoupled to a seismically coupled megathrust, and may explain the slip discrepancy between the seismic and tsunami derived rupture models.

References

Archie, G. E. (1942), The electrical resistivity log as an aid in determining some reservoir characteristics, *Trans. Am. Inst. Min. Metall. Pet. Eng.*, *146*(99), 54–62.

Aubouin, J., J. Bourgois, and J. Azéma (1984), A new type of active margin: The convergent-extensional margin, as exemplified by the Middle America Trench off Guatemala, *Earth Planet. Sci. Lett.*, *67*(2), 211–218.

Bangs, N. L., K. D. McIntosh, E. A. Silver, J. W. Kluesner, and C. R. Ranero (2015), Fluid accumulation along the Costa Rica subduction thrust and development of the seismogenic zone, *J. Geophys. Res.*, *120*, 67–86, doi:10.1002/2014JB011265.

Bassett, D., R. Sutherland, S. Henrys, T. Stern, M. Scherwath, A. Benson, S. Toulmin, and M. Henderson (2010), Three-dimensional velocity structure of the northern Hikurangi margin, Raukumara, New Zealand: Implications for the growth of continental crust by subduction erosion and tectonic underplating, *Geochem. Geophys. Geosyst.*, *11*, Q10013, doi:10.1029/2010GC003137.

Bassett, D., R. Sutherland, and S. Henrys (2014), Slow wavespeeds and fluid overpressure in a region of shallow geodetic locking and slow slip, Hikurangi subduction margin, New Zealand, *Earth Planet. Sci. Lett.*, *389*, 1–13.

Bebout, G. E. (1995), The impact of subduction-zone metamorphism on mantle-ocean chemical cycling, *Chem. Geol.*, *126*(2), 191–218.

Becker, K. (1985), Large-scale electrical resistivity and bulk porosity of the oceanic crust, Deep Sea Drilling Project Hole 504B, Costa Rica Rift, in *Initial Reports of the Deep Sea Drilling Project*, vol. 83, edited by R. N. Anderson, J. Honnorez, and K. Becker, chap. 24., pp. 419–427, U.S. Gov. Print. Off., Washington, D. C.

Beroza, G. C., and S. Ide (2011), Slow Earthquakes and Nonvolcanic Tremor, *Annu. Rev. Earth Planet. Sci.*, *39*(1), 271–296.

Billen, M., E. Cowgill, and E. Buer (2007), Determination of fault friction from reactivation of abyssal-hill faults in subduction zones, *Geology*, *35*(9), 819–822.

Brace, W. F., and A. S. Orange (1968), Electrical resistivity changes in saturated rocks during fracture and frictional sliding, *J. Geophys. Res.*, *73*(4), 1433–1445, doi:10.1029/JB073i004p01433.

Brandon, M. T. (1984), Deformational processes affecting unlithified sediments at active margins: A field study and a structural model, PhD thesis, Univ. of Wash., Seattle, Wash.

Carr, M. J., I. Saginor, G. E. Alvarado, L. L. Bolge, F. N. Lindsay, K. Milidakis, B. D. Turrin, M. D. Feigenson, and C. C. I. Swisher (2007), Element fluxes from the volcanic front of Nicaragua and Costa Rica, *Geochem. Geophys. Geosyst.*, *8*, Q06001, doi:10.1029/2006GC001396.

Clift, P., and P. Vannucchi (2004), Controls on tectonic accretion versus erosion in subduction zones: Implications for the origin and recycling of the continental crust, *Rev. Geophys.*, *42*, RG2001, doi:10.1029/2003RG000127.

Clift, P. D., and A. J. Hartley (2007), Slow rates of subduction erosion and coastal underplating along the Andean margin of Chile and Peru, *Geology*, *35*(6), 503–506.

Collot, J. Y., W. Agudelo, A. Ribodetti, and B. Marcaillou (2008), Origin of a crustal splay fault and its relation to the seismogenic zone and underplating at the erosional north Ecuador–south Colombia oceanic margin, *J. Geophys. Res.*, *113*, B12102, doi:10.1029/2008JB005691.

Conin, M., P. Henry, S. Bourlange, H. Raimbourg, and T. Reuschlé (2011), Interpretation of porosity and LWD resistivity from the Nankai accretionary wedge in light of clay physicochemical properties: Evidence for erosion and local overpressuring, *Geochem. Geophys. Geosyst.*, *12*, Q0AD07, doi:10.1029/2010GC003381.

Constable, S. (2013), Review paper: Instrumentation for marine magnetotelluric and controlled source electromagnetic sounding, *Geophys. Prospect.*, *61*(s1), 505–532.

Constable, S., K. Key, and L. Lewis (2009), Mapping offshore sedimentary structure using electromagnetic methods and terrain effects in marine magnetotelluric data, *Geophys. J. Int.*, *176*(2), 431–442.

Constable, S. C., R. L. Parker, and C. G. Constable (1987), Occam's inversion: A practical algorithm for generating smooth models from electromagnetic sounding data, *Geophysics*, *52*(3), 289–300.

Cowan, D. S. (1985), Structural Styles in Mesozoic and Cenozoic Melanges in the Western Cordillera of North-America, *Geol. Soc. Am. Bull.*, *96*(4), 451–462.

Davis, D., J. Suppe, and F. A. Dahlen (1983), Mechanics of fold-and-thrust belts and accretionary wedges, *J. Geophys. Res.*, *88*(B2), 1153–1172.

De Groot-Hedlin, C. D., and S. C. Constable (1990), Occam's inversion to generate smooth, two-dimensional models from magnetotelluric data, *Geophysics*, *55*(12), 1613–1624.

Dean, S. M., L. C. McNeill, T. J. Henstock, J. M. Bull, S. P. S. Gulick, J. A. Austin, N. L. B. Bangs, Y. S. Djajadihardja, and H. Permana (2010), Contrasting decollement and prism properties over the Sumatra 2004–2005 Earthquake rupture boundary, *Science*, *329*(5988), 207–210.

DeMets, C., R. G. Gordon, and D. F. Argus (2010), Geologically current plate motions, *Geophys. J. Int.*, *181*(1), 1–80.

Dominguez, S., S. Lallemand, J. Malavieille, and R. von Huene (1998), Upper plate deformation associated with seamount subduction, *Tectonophysics*, *293*(3–4), 207–224.

Fisher, D. M., T. W. Gardner, J. S. Marshall, P. B. Sak, and M. Protti (1998), Effect of subducting sea-floor roughness on fore-arc kinematics Pacific coast, Costa Rica, *Geology*, *26*(5), 467–470.

Fitts, T. G., and K. M. Brown (1999), Stress-induced smectite dehydration: Ramifications for patterns of freshening and fluid expulsion in the N. Barbados accretionary wedge, *Earth Planet. Sci. Lett.*, *172*(1), 179–197.

Gaetani, G. A., and T. L. Grove (1998), The influence of water on melting of mantle peridotite, *Contrib. Mineral. Petrol.*, *131*(4), 323–346.

Garcia, E. S., D. T. Sandwell, and K. M. Luttrell (2015), An iterative spectral solution method for thin elastic plate flexure with variable rigidity, *Geophys. J. Int.*, *200*(2), 1010–1026.

Grevemeyer, I., N. Kaul, J. L. Diaz-Naveas, H. W. Villinger, C. R. Ranero, and C. Reichert (2005), Heat flow and bending-related faulting at subduction trenches: Case studies offshore of Nicaragua and Central Chile, *Earth Planet. Sci. Lett.*, *236*(1–2), 238–248.

Hacker, B. R., S. M. Peacock, G. A. Abers, and S. D. Holloway (2003), Subduction factory 2. Are intermediate-depth earthquakes in subducting slabs linked to metamorphic dehydration reactions?, *J. Geophys. Res.*, *108*(B1), 2030, doi:10.1029/2001JB001129.

Harders, R., C. R. Ranero, W. Weinrebe, and J. H. Behrmann (2011), Submarine slope failures along the convergent continental margin of the Middle America Trench, *Geochem. Geophys. Geosyst.*, *12*, Q05S32, doi:10.1029/2010GC003401.

Harris, R. N., G. Spinelli, C. R. Ranero, I. Grevemeyer, H. Villinger, and U. Barckhausen (2010), Thermal regime of the Costa Rican convergent margin: 2. Thermal models of the shallow Middle America subduction zone offshore Costa Rica, *Geochem. Geophys. Geosyst.*, *11*, Q12S29, doi:10.1029/2010GC003273.

Hasterok, D. (2013), A heat flow based cooling model for tectonic plates, *Earth Planet. Sci. Lett.*, *361*, 34–43.

Hayes, G. P., D. J. Wald, and R. L. Johnson (2012), Slab1.0: A three-dimensional model of global subduction zone geometries, *J. Geophys. Res.*, *117*, B01302, doi:10.1029/2011JB008524.

Heesemann, M., I. Grevemeyer, and H. Villinger (2009), Thermal constraints on the frictional conditions of the nucleation and rupture area of the 1992 Nicaragua tsunami earthquake, *Geophys. J. Int.*, *179*(3), 1265–1278.

Hensen, C., K. Wallmann, M. Schmidt, C. R. Ranero, and E. Suess (2004), Fluid expulsion related to mud extrusion off Costa Rica—A window to the subducting slab, *Geology*, *32*(3), 201–204.

Hirschmann, M. M. (2006), Water, melting, and the deep Earth H_2O cycle, *Annu. Rev. Earth Planet. Sci.*, *34*, 629–653.

Hutnak, M., A. T. Fisher, C. A. Stein, R. Harris, K. Wang, E. Silver, G. Spinelli, M. Pfender, H. Villinger, and R. MacKnight (2007), The thermal state of 18–24 Ma upper lithosphere subducting below the Nicoya Peninsula, northern Costa Rica margin, in *The Seismogenic Zone of Subduction Thrust Faults, MARGINS Theoretical and Experimental Earth Science*, edited by T. H. Dixon and J. C. Moore, chap. 4, pp. 86–122, Columbia Univ. Press, New York.

Hyndman, R. D., and S. M. Peacock (2003), Serpentinization of the forearc mantle, *Earth Planet. Sci. Lett.*, *212*(3–4), 417–432.

Ihmlé, P. F. (1996), Frequency-dependent relocation of the 1992 Nicaragua slow earthquake: An empirical Green's function approach, *Geophys. J. Int.*, *127*(1), 75–85.

Jarrard, R. D. (2003), Subduction fluxes of water, carbon dioxide, chlorine, and potassium, *Geochem. Geophys. Geosyst.*, *4*(5), 8905, doi: 10.1029/2002GC000392.

Kameda, J., A. Yamaguchi, S. Saito, H. Sakuma, K. Kawamura, and G. Kimura (2011), A new source of water in seismogenic subduction zones, *Geophys. Res. Lett.*, *38*, L22306, doi:10.1029/2011GL048883.

Kanamori, H., and M. Kikuchi (1993), The 1992 Nicaragua earthquake: A slow tsunami earthquake associated with subducted sediments, *Nature*, *361*(6414), 714–716.

Kastner, M., H. Elderfield, and J. B. Martin (1991), Fluids in convergent margins: What do we know about their composition, origin, role in diagenesis and importance for oceanic chemical fluxes?, *Philos. Trans. R. Soc. London A*, *335*(1638), 243–259.

Key, K. (2009), 1D inversion of multicomponent, multifrequency marine CSEM data: Methodology and synthetic studies for resolving thin resistive layers, *Geophysics*, *74*(2), F9–F20.

Key, K. (2016), MARE2DEM: A 2-D inversion code for controlled-source electromagnetic and magnetotelluric data, *Geophys. J. Int.*, *207*(1), 571–588.

Key, K., and J. Ovall (2011), A parallel goal-oriented adaptive finite element method for 2.5-D electromagnetic modelling, *Geophys. J. Int.*, *186*(1), 137–154.

Key, K., S. Constable, T. Matsuno, R. L. Evans, and D. Myer (2012), Electromagnetic detection of plate hydration due to bending faults at the Middle America Trench, *Earth Planet. Sci. Lett.*, *351*, 45–53.

Kimura, G., and A. Mukai (1991), Underplated units in an accretionary complex—Melange of the Shimanto Belt of Eastern Shikoku, Southwest Japan, *Tectonics*, *10*(1), 31–50.

Kimura, G., et al. (1997), *Proceedings of the Ocean Drilling Program, Initial Reports*, vol. 170, Ocean Drill. Program, College Station, Tex., doi: 10.2973/odp.proc.ir.170.1997.

Kimura, G., S. Hina, Y. Hamada, J. Kameda, T. Tsuji, M. Kinoshita, and A. Yamaguchi (2012), Runaway slip to the trench due to rupture of highly pressurized megathrust beneath the middle trench slope: The tsunamigenesis of the 2011 Tohoku earthquake off the east coast of northern Japan, *Earth Planet. Sci. Lett.*, *339–340*, 32–45.

Kluesner, J. W., E. A. Silver, J. Gibson, N. L. Bangs, K. D. McIntosh, C. R. Ranero, and R. von Huene (2013), High density of structurally controlled, shallow to deep water fluid seep indicators imaged offshore Costa Rica, *Geochem. Geophys. Geosyst.*, *14*, 519–539, doi: 10.1002/ggge.20058.

Langseth, M. G., and E. A. Silver (1996), The Nicoya convergent margin—A region of exceptionally low heat flow, *Geophys. Res. Lett.*, *23*(8), 891–894.

Lauer, R. M., and D. M. Saffer (2015), The impact of splay faults on fluid flow, solute transport, and pore pressure distribution in subduction zones: A case study offshore the Nicoya Peninsula, Costa Rica, *Geochem. Geophys. Geosyst.*, *16*, 1089–1104, doi:10.1002/2014GC005638.

Lay, T., H. Kanamori, C. J. Ammon, K. D. Koper, A. R. Hutko, L. Ye, H. Yue, and T. M. Rushing (2012), Depth-varying rupture properties of subduction zone megathrust faults, *J. Geophys. Res.*, *117*, B04311, doi:10.1029/2011JB009133.

Li, Y., and S. Constable (2007), 2D marine controlled-source electromagnetic modeling: Part 2—The effect of bathymetry, *Geophysics*, *72*(2), WA63–WA71.

Ma, K.-F., E. E. Brodsky, J. Mori, C. Ji, T.-R. A. Song, and H. Kanamori (2003), Evidence for fault lubrication during the 1999 Chi-Chi, Taiwan, earthquake (Mw7.6), *Geophys. Res. Lett.*, *30*(5), 1244, doi:10.1029/2002GL015380.

Matmon, D., and B. A. Bekins (2006), Hydromechanics of a high taper angle, low-permeability prism: A case study from Peru, *J. Geophys. Res.*, *111*, B07101, doi:10.1029/2005JB003697.

McIntosh, K. D., E. Silver, and T. Shipley (1993), Evidence and mechanisms for forearc extension at the accretionary Costa Rica convergent margin, *Tectonics*, *12*(6), 1380–1392.

McIntosh, K. D., E. A. Silver, I. Ahmed, A. Berhorst, C. R. Ranero, R. K. Kelly, and E. R. Flueh (2007), The Nicaragua Convergent Margin: Seismic reflection imaging of the source of a tsunami earthquake, *in The Seismogenic Zone of Subduction Thrust Faults, MARGINS Theoretical and Experimental Earth Science*, edited by T. H. Dixon and J. C. Moore, chap. 9, pp. 257–287, Columbia Univ. Press, New York.

Meng, L., A. Inbal, and J.-P. Ampuero (2011), A window into the complexity of the dynamic rupture of the 2011 Mw 9 Tohoku-Oki earthquake, *Geophys. Res. Lett.*, *38*, L00G07, doi:10.1029/2011GL048118.

Moore, J. C., and P. Vrolijk (1992), Fluids in accretionary prisms, *Rev. Geophys.*, *30*(2), 113–135.

Moore, J. C., J. S. Watkins, T. H. Shipley, K. J. Mcmillen, S. B. Bachman, and N. Lundberg (1982), Geology and tectonic evolution of a juvenile accretionary terrane along a truncated convergent margin—Synthesis of results from Leg-66 of the Deep-Sea Drilling Project, Southern Mexico, *Geol. Soc. Am. Bull.*, *93*(9), 847–861.

Morris, J., R. Valentine, and T. Harrison (2002), Be-10 imaging of sediment accretion and subduction along the northeast Japan and Costa Rica convergent margins, *Geology*, *30*(1), 59–62.

Myer, D., S. Constable, and K. Key (2011), Broad-band waveforms and robust processing for marine CSEM surveys, *Geophys. J. Int.*, *184*(2), 689–698.

Myer, D., S. Constable, K. Key, M. E. Glinsky, and G. Liu (2012), Marine CSEM of the Scarborough gas field, Part 1: Experimental design and data uncertainty, *Geophysics*, *77*(4), E281–E299.

Naif, S., K. Key, S. Constable, and R. L. Evans (2013), Melt-rich channel observed at the lithosphere–asthenosphere boundary, *Nature*, *495*(7441), 356–359.

Naif, S., K. Key, S. Constable, and R. L. Evans (2015), Water-rich bending faults at the Middle America Trench, *Geochem. Geophys. Geosyst.*, *8*, 2582–2597, doi:10.1002/2015GC005927.

Noda, H., and N. Lapusta (2013), Stable creeping fault segments can become destructive as a result of dynamic weakening, *Nature*, *493*(7433), 518–521.

Park, J. O., T. Tsuru, N. Takahashi, T. Hori, S. Kodaira, A. Nakanishi, S. Miura, and Y. Kaneda (2002), A deep strong reflector in the Nankai accretionary wedge from multichannel seismic data: Implications for underplating and interseismic shear stress release, *J. Geophys. Res.*, *107*(B4), doi:10.1029/2001JB000262.

Patino, L. C., M. J. Carr, and M. D. Feigenson (2000), Local and regional variations in Central American arc lavas controlled by variations in subducted sediment input, *Contrib. Mineral. Petrol.*, *138*(3), 265–283.

Peacock, S. A. (1990), Fluid processes in subduction zones, *Science*, *248*(4953), 329–337.

Pichon, X. L., P. Henry, and S. Lallemant (1993), Accretion and erosion in subduction zones: The role of fluids, *Annu. Rev. Earth Planet. Sci.*, *21*, 307–331.

Platt, J. P., J. K. Leggett, J. Young, H. Raza, and S. Alam (1985), Large-scale sediment underplating in the Makran Accretionary Prism, Southwest-Pakistan, *Geology*, *13*(7), 507–511.

Pytte, A. M., and R. C. Reynolds (1989), The thermal transformation of smectite to illite, in *Thermal History of Sedimentary Basins: Methods and Case Histories*, edited by N. D. Naeser and T. H. McCulloh, chap. 8, pp. 133–140, Springer, New York.

Ranero, C. R., and R. von Huene (2000), Subduction erosion along the Middle America convergent margin, *Nature*, *404*(6779), 748–752.

Ranero, C. R., R. von Huene, E. Flueh, M. Duarte, D. Baca, and K. McIntosh (2000), A cross section of the convergent Pacific margin of Nicaragua, *Tectonics*, *19*(2), 335–357.

Ranero, C. R., I. Grevemeyer, H. Sahling, U. Barckhausen, C. Hensen, K. Wallmann, W. Weinrebe, P. Vannucchi, R. von Huene, and K. McIntosh (2008), Hydrogeological system of erosional convergent margins and its influence on tectonics and interplate seismogenesis, *Geochem. Geophys. Geosyst.*, *9*, Q03S04, doi:10.1029/2007GC001679.

Revil, A., L. M. Cathles III, S. Losh, and J. A. Nunn (1998), Electrical conductivity in shaly sands with geophysical applications, *J. Geophys. Res.*, *103*(B10), 23,925–23,936.

Saffer, D. M., and B. A. Bekins (2002), Hydrologic controls on the morphology and mechanics of accretionary wedges, *Geology*, *30*(3), 271–274.

Saffer, D. M., and H. J. Tobin (2011), Hydrogeology and mechanics of subduction zone forearcs: Fluid flow and pore pressure, *Annu. Rev. Earth Planet. Sci.*, *39*(1), 157–186.

Saffer, D. M., and L. M. Wallace (2015), The frictional, hydrologic, metamorphic and thermal habitat of shallow slow earthquakes, *Nat. Publ. Group*, *8*(8), 594–600.

Sahling, H., D. G. Masson, C. R. Ranero, V. Hühnerbach, W. Weinrebe, I. Klaucke, D. Bürk, W. Brückmann, and E. Suess (2008), Fluid seepage at the continental margin offshore Costa Rica and southern Nicaragua, *Geochem. Geophys. Geosyst.*, *9*, Q05S05, doi:10.1029/2008GC001978.

Sak, P. B., D. M. Fisher, T. W. Gardner, J. S. Marshall, and P. C. LaFemina (2009), Rough crust subduction, forearc kinematics, and Quaternary uplift rates, Costa Rican segment of the Middle American Trench, *Geol. Soc. Am. Bull.*, *121*(7–8), 992–1012.

Sallarès, V., A. Meléndez, M. Prada, C. R. Ranero, K. McIntosh, and I. Grevemeyer (2013), Overriding plate structure of the Nicaragua convergent margin: Relationship to the seismogenic zone of the 1992 tsunami earthquake, *Geochem. Geophys. Geosyst.*, *14*, 3436–3461, doi:10.1002/ggge.20214.

Sample, J. C., and D. M. Fisher (1986), Duplex accretion and underplating in an ancient accretionary complex, Kodiak Islands, Alaska, *Geology*, *14*(2), 160–163.

Santelli, C. M., B. N. Orcutt, E. Banning, W. Bach, C. L. Moyer, M. L. Sogin, H. Staudigel, and K. J. Edwards (2008), Abundance and diversity of microbial life in ocean crust, *Nature*, *453*(7195), 653–656.

Satake, K. (1994), Mechanism of the 1992 Nicaragua Tsunami Earthquake, *Geophys. Res. Lett.*, *21*(23), 2519–2522.

Satake, K., and Y. Tanioka (1999), Sources of tsunami and tsunamigenic earthquakes in subduction zones, *Pure Appl. Geophys.*, *154*(3–4), 467–483.

Scherwath, M., et al. (2010), Fore-arc deformation and underplating at the northern Hikurangi margin, New Zealand, *J. Geophys. Res.*, *115*, B06408, doi:10.1029/2009JB006645.

Scholz, C. H. (1998), Earthquakes and friction laws, *Nature*, *391*(6662), 37–42.

Screaton, E., D. Saffer, P. Henry, and S. Hunze (2002), Porosity loss within the underthrust sediments of the Nankai accretionary complex: Implications for overpressures, *Geology*, *30*(1), 19–22.

Sen, P. N., and P. A. Goode (1992), Influence of temperature on electrical conductivity on shaly sands, *Geophysics*, *57*(1), 89–96.

Shipley, T. H., K. D. McIntosh, E. A. Silver, and P. L. Stoffa (1992), Three-dimensional seismic imaging of the Costa Rica accretionary prism: Structural diversity in a small volume of the lower slope, *J. Geophys. Res.*, *97*(B4), 4439–4459.

Silver, E. A., M. J. Ellis, N. A. Breen, and T. H. Shipley (1985), Comments on the growth of accretionary wedges, *Geology*, *13*(1), 6–9.

Spinelli, G. A., and M. B. Underwood (2004), Character of sediments entering the Costa Rica subduction zone: Implications for partitioning of water along the plate interface, *Island Arc*, *13*(3), 432–451.

Spinelli, G. A., D. M. Saffer, and M. B. Underwood (2006), Hydrogeologic responses to three-dimensional temperature variability, Costa Rica subduction margin, *J. Geophys. Res.*, *111*, B04403, doi:10.1029/2004JB003436.

St Clair, J., W. S. Holbrook, H. J. A. Van Avendonk, and D. Lizarralde (2016), Along-strike structure of the Costa Rican convergent margin from seismic a refraction/reflection survey: Evidence for underplating beneath the inner forearc, *Geochem. Geophys. Geosyst.*, *17*, 501–520, doi:10.1002/2015GC006029.

Staudigel, H. (2014), Chemical fluxes from hydrothermal alteration of the oceanic crust, in *Treatise on Geochemistry*, edited by K. K. Turekian and H. D. Heinrich, 2 ed., chap. 4.16, pp. 583–606, Elsevier, Oxford, U. K.

Thompson, A. B. (1992), Water in the Earths upper mantle, *Nature*, *358*(6384), 295–302.

Tryon, M. D., C. G. Wheat, and D. R. Hilton (2010), Fluid sources and pathways of the Costa Rica erosional convergent margin, *Geochem. Geophys. Geosyst.*, *11*, Q04S22, doi:10.1029/2009GC002818.

Vannucchi, P., D. W. Scholl, M. Meschede, and K. McDougall-Reid (2001), Tectonic erosion and consequent collapse of the Pacific margin of Costa Rica: Combined implications from ODP Leg 170, seismic offshore data, and regional geology of the Nicoya Peninsula, *Tectonics*, *20*(5), 649–668.

Vannucchi, P., S. Galeotti, P. D. Clift, C. R. Ranero, and R. von Huene (2004), Long-term subduction-erosion along the Guatemalan margin of the Middle America Trench, *Geology*, *32*(7), 617–620.

Von Huene, R., and S. Lallemand (1990), Tectonic erosion along the Japan and Peru convergent margins, *Geol. Soc. Am. Bull.*, *102*(6), 704–720.

Von Huene, R., and D. W. Scholl (1991), Observations at convergent margins concerning sediment subduction, subduction erosion, and the growth of continental crust, *Rev. Geophys.*, *29*(3), 279–316.

Von Huene, R., C. R. Ranero, and P. Vannucchi (2004a), Generic model of subduction erosion, *Geology*, *32*(10), 913–916.

Von Huene, R., C. R. Ranero, and P. Watts (2004b), Tsunamigenic slope failure along the Middle America Trench in two tectonic settings, *Mar. Geol.*, *203*(3–4), 303–317.

Wada, I., K. Wang, J. He, and R. D. Hyndman (2008), Weakening of the subduction interface and its effects on surface heat flow, slab dehydration, and mantle wedge serpentinization, *J. Geophys. Res.*, *113*, B04402, doi:10.1029/2007JB005190.

Walther, C. H. E., E. R. Flueh, C. R. Ranero, R. von Huene, and W. Strauch (2000), Crustal structure across the Pacific margin of Nicaragua: Evidence for ophiolitic basement and a shallow mantle sliver, *Geophys. J. Int.*, *141*(3), 759–777.

Wang, K., and Y. Hu (2006), Accretionary prisms in subduction earthquake cycles: The theory of dynamic Coulomb wedge, *J. Geophys. Res.*, *111*, B06410, doi:10.1029/2005JB004094.

Waxman, M. H., and L. J. M. Smits (1968), Electrical conductivities in oil-bearing shaly sands, *Soc. Pet. Eng. J.*, *8*(2), 107–122.

Weinrebe, W., and C. R. Ranero (2012), Multibeam Bathymetry Compilation of the Central America Pacific Margin, Integrated Earth Data Applications (IEDA), Lamont-Doherty Earth Observatory of Columbia University, doi:10.1594/IEDA/100069.

Wheelock, B., S. Constable, and K. Key (2015), The advantages of logarithmically scaled data for electromagnetic inversion, *Geophys. J. Int.*, *201*(3), 1765–1780.

Wilson, C. R., M. Spiegelman, P. E. van Keken, and B. R. Hacker (2014), *Earth and planetary science letters, Earth Planet. Sci. Lett.*, *401*(C), 261–274.

Worzewski, T., M. Jegen, H. Kopp, H. Brasse, and W. T. Castillo (2010), Magnetotelluric image of the fluid cycle in the Costa Rican subduction zone, *Nat. Geosci.*, *4*(2), 108–111.

Yao, H., P. Gerstoft, P. M. Shearer, and C. Mecklenbräuker (2011), Compressive sensing of the Tohoku-Oki Mw 9.0 earthquake: Frequency-dependent rupture modes, *Geophys. Res. Lett.*, *38*, L20310, doi:10.1029/2011GL049223.

Ye, L., T. Lay, and H. Kanamori (2013), Large earthquake rupture process variations on the Middle America megathrust, *Earth Planet. Sci. Lett.*, *381*, 147–155.